Deposition and erosion of a Light-Toned Yardang-forming unit of Mt Sharp, Gale crater, Mars

G. Dromart, Laetitia Le Deit, W. Rapin, O. Gasnault, S. Le Mouélic, C. Quantin-Nataf, N. Mangold, D. Rubin, J. Lasue, S. Maurice, et al.

Deposition and Erosion of a Light-Toned Yardang-forming Unit of Mt Sharp, Gale Crater, Mars

G. Dromart[1], L. Le Deit[2], W. Rapin[3], O. Gasnault[4], S. Le Mouélic[2], C. Quantin-Nataf[5], N. Mangold[2], D. Rubin[6], J. Lasue[4], S. Maurice[4], H.E. Newsom[7], P. Pinet[4], L. Scuderi[8], R.C. Wiens[9].

Highlights:

- Using the novel "long distance" capability of the Remote Micro Imager of ChemCam
- Amalgamated eolian deposits compose the Light-Toned Yardang Unit of Mt Sharp
- Exposed yardang forms of Mt Sharp are paleo geomorphic features
- A likely global climate change at the Early-Late Hesperian Transition on Mars
- Exhumed yardangs are relevant supports to study paleo-climatic conditions on Mars

Deposition and Erosion of a Light-Toned Yardang-forming Unit of Mt Sharp, Gale Crater, Mars

G. Dromart[1], L. Le Deit[2], W. Rapin[3], O. Gasnault[4], S. Le Mouélic[2], C. Quantin-Nataf[5], N. Mangold[2], D. Rubin[6], J. Lasue[4], S. Maurice[4], H.E. Newsom[7], P. Pinet[4], L. Scuderi[8], R.C. Wiens[9].

[1]Univ Lyon, ENSL, Univ Lyon 1, CNRS, LGL-TPE, 69364 Lyon, France

[2]Univ Nantes, CNRS, LPG, 44322 Nantes, France

[3]California Institute of Technology, GPS, Pasadena, California, CA 91125, USA

[4]Univ Toulouse, CNRS, CNES, IRAP, 31400 Toulouse, France

[5]Univ Lyon, Univ Lyon 1, ENSL, CNRS, LGL-TPE, 69622 Villeurbanne, France

[6]University of California Santa Cruz, Earth and Planetary Sciences, Santa Cruz, CA 95064, USA

[7]University of New Mexico, Institute of Meteoritics, Albuquerque, NM 87131, USA

[8]University of New Mexico, Department of Earth & Planetary Sciences, Albuquerque, NM 87131, USA

[9]Los Alamos National Laboratory, Los Alamos, NM 87544, USA

Abstract. Gale crater is a large impact crater with a ca 5 km thick sequence of stratified rocks in it, expressed today as a central eroded mound (i.e., Aeolis Mons informally named Mt. Sharp). A goal of the current Mars Science Laboratory mission in Gale crater is to investigate the processes that deposited, lithified, and eroded this fill. The Light-Toned Yardang Unit (LTYu) unit, the subject of the present research, is one of the geological units of Mt Sharp. Our specific purpose here is to refine and interpret the imaging documentation of the morphologic and stratal components of the LTYu, at large outcrop scale. In combination with established orbital images, we use the *Remote Micro-Image*r (RMI) of *ChemCam*, a remote sensing instrument currently operated onboard *Curiosity* rover, which provides several types of context imaging. RMI capabilities now include "Long Distance" acquisitions of targets several kilometers away. In these new acquisitions, substantial differences are visible in LTYu yardang attitudes from lowest to uppermost elevations allowing tentative subdivision of the LTYu into subunits. Bedding geometries in the lower LTYu are consistent with eolian dune foresets which collectively prograde towards an average N134° direction. Based on stratal architectures, the LTYu is viewed as an amalgamated stack of at least two, and possibly four, ancient erg systems bounded by large deflationary "supersurfaces". Observations point to a multistory generation of yardangs interpreted to have been successively buried during the stratigraphic building of Mt Sharp. We conclude that the successive sequences of eolian deposition-erosion recorded by the LTYu have been generated by cyclic changes from semi-arid to arid conditions, coupled in climatic cycles, including wind regime change. The regional unconformity that tops the Lower mound formation of Mt Sharp, and the subsequent emplacement of the LTYu, collectively express a clear tendency toward sustained arid environments for this region of Mars around the Early – Late Hesperian transition. Given the large time scale involved (i.e., a few tens of million years as a minimum), we consider it likely that the local evidence for increased aridity in the Mt Sharp stratigraphy is a manifestation of climate change affecting the whole planet.

Keywords. Mars Climate, Gale Crater, Yardang, Stratigraphy, Eolian, ChemCam

1. Introduction.

Gale crater is a member of a broad family of impact craters referred to as "Overfilled" (Grotzinger and Milliken, 2012), namely craters that have thousands of meters of layered fill materials, and whose uppermost parts approach or exceed the elevation of the crater margins. In Gale crater, the sequence of stratified rocks occurs today as an eroded mound (i.e., Aeolis Mons informally named Mt. Sharp). One of the goals of the current Mars Science Laboratory (MSL) in Gale is to investigate the processes that deposited, lithified, and subsequently eroded this fill. Mt Sharp's origin has been the subject of considerable discussion, with various hypotheses including pyroclastic deposits (e.g., Scott and Chapman, 1995), lacustrine deposits (e.g., Malin and Edgett, 2000), and an eolian origin (Bridges et al., 2010; Kite et al., 2013; Anderson et al., 2018).

The bright unit exposed on the western flank of Mt Sharp, termed the "Light-Toned Yardang Unit" (LTYu; Anderson & Bell, 2010), is the focus of this study. LTYu, one of the geological units that build up Mount Sharp (Le Deit et al., 2013), lies at the boundary of the Lower and Upper formations of the Gale crater fill. It is unconformable with the Lower formation (Malin and Edgett, 2000; Anderson and Bell, 2010), and is in turn onlapped by the Upper mound formation (Le Deit et al., 2013). LTYu was originally described (Malin and Edgett, 2000) as a massive, light-toned unit, the surface of which is dominated by large, sharply-tapered ridges and intervening furrows. Anderson and Bell (2010), using the Mars Reconnaissance Orbiter (MRO) Context Camera (CTX), reported LTYu as a high albedo, uncratered feature. It was then mapped as unit "ume3" by Thomson et al. (2011) and "Cyu" by Le Deit et al. (2013). Anderson & Bell (2010) concluded that scalloped texture of the yardang-forming material of the LTYu suggests that it is soft enough for eolian erosion to scour shallow pits into the surface. Le Deit et al. (2013) proposed that the LTYu might correspond to airfall sediments and wind-blown sands.

Our purpose is to refine our understanding of the morphologic and stratal components of Gale crater's LTYu, at large outcrop scale, to reconstruct paleo- depositional and erosional environments, and to decipher the termination scenario of the aqueous story of Gale crater. We used the RMI (Remote Micro-

Imager) of ChemCam in combination with the visible CTX and HiRISE (High Resolution Imaging Science Experiment) data of MRO. The RMI, a remote sensing instrument currently operated onboard Curiosity rover, provides several types of context imaging, newly including "Long Distance" acquisitions of targets several kilometers away. The paper presents the geologic evidence derived from this imagery for a genetic model of multistory deposition – early erosion of the LTYu by winds. The paper discusses the role of water in LTYu deposition/preservation, the timing and duration of LTYu emplacement, and the timing of yardang formation. It closes with remarks about possible atmospheric conditions in Gale crater at the Early -Late Hesperian Transition.

2. Geological context

Gale crater, a ca 155 km diameter impact crater, is located near the martian equateur (5°S/138°E; Fig. 1), at the planet's crustal dichotomy. The crater contains a thick, ca 5 km, sequence of stratified rocks that make up the central mound, the maximum elevation of which is similar to that of the southern crater rim but which is several kilometers higher than the degraded northern rim (Fig. 1A). Based on crater distributions on the Gale ejecta blanket, Gale crater formed 3.7 ± 0.1 Ga ago (Thomson et al., 2011; Le Deit et al., 2013) at the Noachian-Hesperian transition. The early degradation of the crater rim supplied sediments which prograded away from the rim, aggrading an episodically filled lake basin (Grotzinger et al., 2015). This lake system likely intermittently existed for thousands to millions of years implying a wet climate. The complete sequence of filling Gale crater and exhumation of Mt Sharp largely happened within a few hundred million years after Gale crater formed (i.e., by the end of Hesperian times) (Thomson et al. (2011).

Curiosity landed in the northwestern crater floor of Gale crater (Vasavada et al., 2014), and has traversed >7 km to reach the lower units of Mt. Sharp. The dark-toned, nearly flat-lying layers of the lower units yield orbital spectral signatures of phyllosilicates, mono and polyhydrated sulfates, and ferric oxide (hematite) (Milliken et al., 2010; Fraeman et al., 2016). From observations by Curiosity, the thick, ca

400 m, sequence of the lower units has been inferred to consist of fluvio-lacustrine deposits (e.g., Grotzinger et al., 2015).

Higher on Mt Sharp, well above even the future traverse of Curiosity, the LTY-forming material is a distinctive, high CTX albedo feature well exposed on the northwest flank of the Gale crater mound (Fig. 1). From orbit, the LTYu displays a general lens-shape that covers an area of about 70 km^2. In CTX images, the material appears to be a massive deposit, with a surface that has been eroded into yardang-like forms. Infrared CRISM spectral signatures of LTYu typically are those of the ubiquitous Martian dust with a very weak sulfate signature detected locally (Milliken et al., 2010; Thomson et al., 2011).

The LTYu lies along a ca 15° slope between -3990 and -1674 m, clearly and unconformably overlying the lower units of Mt Sharp, namely the Syu1 unit (Small yardang unit 1; Le Deit et al., 2013), as demonstrated by a crater partially exhumed from beneath the LTYu (Malin and Edgett, 2000; Fig. 1B). The relationships of the LTYu with the Syu1, and the observation made by Le Deit et al. (2013, fig. 13b) that the topmost yardang forms of the LTYu are buried by a set of continuous, planar strata of the Small yardang unit 2 (Syu2) (i.e., lower Upper Mound unit of Anderson and Bell, 2010) supports an interpretation that the LTYu occurs as a stratigraphic unit enclosed in the Upper mound formation, and not as a distinct, more recent formation patched on the flank of a previously eroded central mound. According to Le Deit et al. (2013), the LTYu is a thin stratigraphic unit (i.e., 100 to 200 m) which was emplaced at the Early – Late Hesperian transition.

The Benched unit (Bu; Fig. 1B), a thick stratigraphic package of Mt Sharp characterized by a more uniform albedo and large-scale cliff-bench style geomorphic expression in some areas, lies above the LTYu and the Syu2 (Anderson et al., 2018).

3. Data sets and methods

3.1. Orbital camera data

Orbital visible images were used: to provide the general geological and geomorphological contexts of the LTYu; measure contact geometries of stratigraphic units; measure the morphological aspect of distinct yardang-bearing subunits; delineate the bedding geometry of the deposits and; provide context for Long Distance RMI (LD RMI) views from Curiosity rover.

We used the basemap generated for science and engineering operations conducted by the MSL Curiosity rover (https://bit.ly/MSL_Basemap). The basemap and associated DTM (Digital Terrain Model) were built from two types of visible images: CTX, for which there is an extensive coverage at 6 m/pixel; and ~0.27 m/pixel data from the HiRISE instrument. Where available, we used ultra-highly resolved HiRISE stereo images derived DTMs (1 m) (Kirk et al., 2008) to measure the geometry of contacts and beds, and to project the ground LD RMI images over the topography.

Morphometric attributes of the ridges were measured manually using *Adobe Illustrator*® software applied to MOLA (Mars Orbiter Laser Altimeter) DTM elevations. We did not consider the attitudes of all individual ridges and restricted our measurements to larger forms (i.e., length >30 m) because positioning is too uncertain and measurements are too inaccurate for small features. Accordingly, the analysis does not yield the comprehensive distribution of the forms. However, this method, repeatedly applied across the whole LTYu, was sufficient to disclose salient differences between morpho-stratigraphic subunits of the LTYu. To evaluate the accuracy of our method, a second operator repeated measurements on 39 ridges of the lower part of the LTYu. Results show that: (i) average of direction differences was minimal (i.e., 1.95°) between observers but individual differences up to 10° occurred; (ii) the magnitude of the relative errors on measured lengths and widths is ± 5%.

ArcGIS® extension Layer Tools (Kneissl et al., 2010) were used to quantify the geometry of the LTYu basal bounding surface. This tool combines spatial coordinates of measured points from imagery with corresponding elevation values extracted from an underlying DTM. X,Y,Z data from measurements along a geologic contact allow construction of planes describing the extent of the geological surface of interest. The surface is defined in terms of planar dip and dip direction by at least three measurement

points. For more than three points, the best-fitting plane is computed using a polynomial fit. Output from tool comprises dip-angle and dip-direction values of the interpolated planes.

3.2. Ground visible data: Long Distance Remote Micro-Imager (LD RMI) images

It is difficult to interpret stratal architectures of a deposit (e.g., bedding geometries and truncations) based purely on the plan view provided by orbital data. Accordingly, we used a ground camera (RMI) which allows cross-sectional views of strata. ChemCam's RMI instrument affords the finest pixel scale on the rover mast with 19.6 µrad/pixel (Le Mouélic et al., 2015). The RMI telescope was originally designed to provide close-in context images for LIBS analyses. After the loss of the Continuous Wavelength Laser function, which focused the RMI telescope, an autofocus procedure was implemented that offers the advantage of being operational at all distances, including imaging of targets up to several kilometers away (Peret et al., 2016; SM_Text 1).

The smallest features that can be distinguished at the center of these LD RMI images at best focus range between [6 - 10] cm at 1 km. At 5 km the finest resolution [0.3 - 0.5] m is equivalent to HiRISE orbital resolution. Usually a series of individual LD RMI images is acquired with an appropriate offset between images (6 to 12 mrad) which ensures an overlap of the images and the full coverage of the target. The individual images are stitched into mosaics and then subjected to corrections to improve, for example, the image sharpness (SM_Text 1).

Using the *Visibility Tool* of *ArcMap*®, LD RMI mosaics are projected as view sheds onto the DTMs. The projection ensures the control of projective geometry issues associated with the LD RMI mosaics, and facilitates the calculation of the elevation range of the targets.

4. Observations

4.1. Morphological elements

From orbit, much of the light-toned material surface is textured by variably contiguous low ridges and shallow depressions (Fig. 2). These ridges are several tens to a few hundred meters-long, with a large aspect ratio (length/width) ≥ 4:1 (SM_Table 1). Local relief between crests and troughs ranges from 5 to 25-30 meters. However, the pattern of the forms is not homogeneous across the LTYu (Fig. 2). Based on substantial textural differences that appear from the western to eastern exposures (i.e., from the lowest to uppermost elevations) the surface of the LTYu can be tentatively subdivided into four (4) subunits (Fig. 2): Lower LTY; Middle LTY; Upper LTY, and Top LTY.

The clearest morphological difference is in between the stepped topography of the lower subunit ridges, and the variably elongated, lens-shaped pattern of the morphologies of the upper subunits. The lower stepped pattern results from the intersection of three straight ridge crest directions. It yields distinct dissected alignments of triangular facets in plan view, with a smooth, gently sloping flank, and a steep, cliff-forming side (i.e., transversally asymmetric profiles) (Figs 2B, 4A). Cross-sectional RMI views show that the Lower LYTu is made up of a stack of ~10 m-thick, light-toned, resistant, clearly-dipping (i.e., apparent dip up to 12°SW) elongated forms (i.e., ridges) separated by recessive horizons (Fig. 4C).

The upper subunits display forms that can be distinguished according to the number and distribution of the long-axis direction of the ridges (Fig. 2; SM_Table 1), and from geometric characteristics of the forms observed in plan view (Fig. 2C, D, E). Forms of the Middle LTY subunit show teardrop-like morphologies with blunt heads and convex, broad tapered tails. The forms of the Upper LTY subunit are rhomboidal in shape and exhibit variably flattened crests lines. It is difficult to separate individual forms from each other in the Upper LTY subunit because the larger forms are themselves dissected into "self-similar" smaller forms, giving way to a quasi "braided" pattern. The forms of the Top LTY subunit present streamlined ridges with steep and narrow flanks, separated by flat-floored troughs.

4.2. Basal unconformity

Thomson et al. (2011) determined the attitude of the contact between the LTYu and the surrounding units by identifying intersections between mapped outline of the entire LTYu and topographic profiles from MOLA data. They concluded that the contact is best described by a planar surface with a strike

and dip of N45°E, 12.1°_NW (i.e., inclined to the NW). However, the means by which the geometry of the basal surface of the LTYu has been reconstructed cannot be adopted: the bounding surface of the southeastern LTYu is clearly overlain by the Upper mound formation, namely by the Syu2 unit of Le Deit et al. (2013; fig. 13b), and is thus the top surface of the LTYu, and not its basal surface. We here restricted the measurement of the contact attitude to the western part of the LTYu, an area where the unconformable relationship of the LTYu with the underlying unit is clearly exposed. This surface dips to the northwest (N53°-55°E strike direction), with locally variable angles increasing from 6.5° in the southern section of the contact to 15.5° in the northern section (Fig. 3A).

Close-ups of HiRISE images that cover the contact show that a paleo-crater has been stripped off and filled prior to the deposition of the LTYu (i.e., partially-exhumed crater of figure 3C). As well, a series of ridges and troughs forms at the top of the upper Syu1, are buried by the lowermost LTYu deposits (Fig. 3B).

4.3. Stratal components of the Lower LTYu

Stratal architectures were analyzed for the lower LTY subunit only, for which we have both the RMI and HiRISE images that can advantageously be combined (Fig. 4). Ground and orbital imagery (Fig. 5 & 6) reveal well-exposed, and extensive straight bed traces. Cross-sectional views reveal that the resistant ridges are internally composed of sets of gently dipping to sub-horizontal, mostly planar, evenly stacked individual beds (Fig. 5). Only a few examples of erosional stratigraphic surfaces intersecting the modern slope have been identified (i.e., local surfaces that bound bed sets apparently truncating other bed sets). Orbital plan views (Fig. 6) show bed traces running approximately parallel with apparent uniform spacing. These traces have a linear to curvilinear pattern that suggests prevalent planar geometry for the beds. Collectively, figures 5 & 6 reveal that the beds are arranged as shingled prograding clinobeds. The strike azimuth of the bed traces in plan view is fairly steady, around the average direction of N44°. It can thus be inferred that the clinobeds dip towards the southeast, which would be the dominant direction of the net sediment transport.

225 5. A model: Multistory deposition-erosion by winds

226 5.1. Deposition/preservation of the Lower LTY subunit

227 In the Lower LTYu-composing material, observed dips, and the very finely- and evenly-bedding
228 geometries are interpreted as strike sections of individual strata (Fig. 5) that collectively prograde
229 towards a N134° direction (Fig. 6). The large lateral extension and planarity of these now-variably-
230 eroded dipping beds, together with low variation in bed dip azimuths in orbital imagery (Fig. 6)
231 collectively are consistent with eolian dune foresets. Moreover, the fact that some resistant beds are
232 uniformly spaced (i.e., alternating with recessive interbeds), at the toe of the ridge-form in particular,
233 points to cyclic bed deposition, which is a characteristic feature of eolian tracts. Conversely, counter
234 dipping beds that would point to the development of antidune systems, typical of pyroclastic flow
235 deposits, or extensive draping ashfall beds have not been observed.
236
237 The unscaled, two-dimensional model we propose for deposition and preservation of the bed sets of the
238 Lower LTY subunit (Fig. 7) is derived from the application to our observations of the theoretical model
239 of Kocurek (1986). The theoretical diagram (SM_Fig.1A) describes the generation of sets of cross-strata
240 by migrating and climbing eolian dunes. These cross-strata sets are bounded by surfaces referred to as
241 first-order surfaces. The theoretical model is derived from a wealth of examples available in the
242 terrestrial stratigraphic record (e.g., the Jurassic Navajo Sandstones in Zion National Park; SM_Fig.1B).
243
244 By extension, it is speculated that the model of net deposition for the Lower LTY subunit applies to the
245 entire LTYu. The main strength for the LTYu model as a multistory deposition-deflation by wind, lies
246 in the fact it assimilates all of the observations we have, which derive from a synergetic analysis of well-
247 resolved orbital and ground data. Conversely, a potential weakness of the model is that it is also
248 supported by negative evidence, namely observations that do not fit alternative interpretation such as
249 tephra, or fluvial deposition.
250

There is some inadequacy of directly supporting observables for wind interpretation, and a definite point of weakness lies in the limitation in the number and quality of appropriate observables, namely: (i) the dataset is not homogeneous across the object of analysis (i.e., LD RMI and HiRISE stereo DEM's are only available for the Lower LTY subunit), so the fine stratal organization of the upper LTY subunits cannot be determined; (ii) our dataset derives from remote analysis and sorely lacks small scale in-situ outcrop observation. For example, documentation of the development of several superimposed orders of stratification and cyclicity (uniform vertical spacing of beds and first-order bounding surfaces), which is typical and diagnostic of eolian deposits, cannot be really achieved and is only suspected here. Likewise, even if our model predicts accumulation in dry eolian systems because of the apparent absence of interdune elements, we cannot rule out wet interdunes from the RMI images alone, because a lot of eolian sandstones have indications of wet interdunes only when viewed from a few meters away (e.g., crinkly laminae formed by alternating wetting and drying and/or precipitation and dissolution of evaporites within lowermost foresets or in the strata immediately underlying the bounding surfaces; Irmen & Vondra, 2000). Another aspect of the lack of control at the small outcrop scale is that we are unable to confirm the model-predicted occurrences of uniformly -spaced, quasi-planar, ramping-up truncation surfaces (i.e., first-order surfaces; SM_Fig. 1) within the Lower LTYu. This may be due to the propensity the first-order bounding surfaces have to lie in recessive intervals, and so are often covered by scree.

5.2. Stratigraphic geometries of the upper LTY subunits

As for the upper LTY subunits as a whole, we propose a geometric model for the net deposits (Fig. 8A). The graphic model is a stratigraphic cross-section derived from the orbital plan views. The four (4) LTYu subunits that have been distinguished from the attitudes of the morphological elements (Fig. 2) are parallel bands that intersect the general slope of the LTYu. We believe that these morphological units express stratigraphic entities separated by discontinuities. Supporting evidence for this interpretation comes from the fact that the lines that bound the LTY subunits appear to run roughly parallel with the basal unconformity (SM_Fig.2). Conversely, a weakness of this model arises from the

fact that the contacts between the LTY stratigraphic subunits, referred to as sub-unconformities, appear from orbit as amorphous features and generally, with probable exception of the contact between the Lower LTY and the Middle LTY subunits (SM_Fig. 3), cannot not clearly be delineated. The poor delineation of the contacts may come from non-optimal HiRISE camera angles, weak low rock tonality contrasts, or possibly because these contact surfaces are paraconformities (i.e., similar bedding attitude on both sides of the discontinuity).

Interpretation of wind-influenced control of internal sub-unconformities of the LTYu is derived from two observations. First, the characteristics of the major basal contact geometry **(**i.e., truncation of underlying strata, declivity between 6-15°, minimal elevation difference of about 1 km) collectively are inconsistent with a simple subaqueous depositional process and fits well with eolian control of the erosional surface. Second, sub-unconformities that bound LTY stratigraphic subunits are parallel with the basal unconformity, a feature consistent with large eolian deflationary surfaces.

There are wealth of analogs in the eolian terrestrial record of stratigraphic organizations similar to those depicted here for the LTYu. The bounding surfaces of the LTYu (i.e., internal sub-unconformities of the LTYu) show a minimal extension of several kilometers with separate packages of LTY material of 100-300 meters in thickness (Fig. 8A). A gross terrestrial analog for these surfaces is available in Western USA basins where, in some localities, Paleozoic and Mesozoic vertical stacks of eolian genetic sequences are bounded by extensive (tens of kilometers) surfaces that are relatively flat, and at angular discordance with the first-order surfaces. These large, regional surfaces have been called "super bounding surfaces" (Kocurek, 1988) or "supersurfaces" (Brookfield, 1992). An excellent example is the succession observed in southern Utah where the stratigraphic column in order shows a sequence of: Navajo Sandstone (100 - 600 m) - J1 Unconformity - Temple Cap Sandstone (50 - 100 m) - J2 Unconformity - Page Sandstone (20 - 60 m) (Blakey et al., 1988; 1996). The major unconformity underlying the LTYu and sub-unconformities within the LTYu collectively are herein interpreted to be super bounding surfaces, even though their geometry is not horizontal and their areal development is apparently much more limited than that found in the Earth basin referred to here. We think these differences are due to the unique position of the eolian LTYu system on the flank of a paleo-mound.

306

307 5.3. Yardang formation

308

309 Yardangs are spectacular erosional landforms found in major terrestrial deserts globally. They often
310 occur as great fields up to a few tens of millions of km^2 in extent (e.g., McCauley et al., 1977). Satellite
311 imagery analysis coupled with field studies show yardangs to be relatively straight, elongate,
312 asymmetric spurs sculpted upon variably lithified and aged material (e.g., El-Baz et al., 1979; Wang et
313 al., 2018). Numerous recent surveys have addressed terrestrial yardang forms (e.g., Laity, 2011; Zhao
314 et al., 2018). The consensus is that the prerequisites for yardang development are strong, unidirectional
315 or reversing winds in arid regions over barren continuous rock exposures or over the surfaces of poorly
316 consolidated sediment. The studies have found that the long, shallow troughs separating yardangs are
317 locations where most of erosion takes place. On Mars, yardangs were observed in the earliest orbiter's
318 images (e.g., McCauley, 1973; Ward, 1979) with these forms typically occurring in equatorial regions,
319 including in particular the extensive Medusae Fossae Formation (MFF), east of Tharsis (e.g., Mandt et
320 al., 2008).

321

322 Surface elements of the Gale central mound LTYu are interpreted as yardangs because of the
323 morphological similarity they share with the terrestrial yardangs (e.g., teardrop-like morphologies of the
324 Middle LTY subunit closely fit the *whaleback* type yardangs defined by Wang et al., 2018). The shape
325 of these troughs by wind is very likely and alternative formation processes (gravity-driven erosion
326 by mass and fluvial flows) are precluded because: (i) the overall direction of the modern slope is toward
327 the NW, in distinct contrast to the primary direction of erosional features that run parallel to the main
328 yardang's axes (Fig. 2; SM_Table 1); and (ii) valleys in between the yardangs crests appear not to be
329 fan-terminated downslope.

330

331 We hypothesize that the LTYu yardang's ultimate morphology results from the dual influence between
332 the original bedding geometries and the primary direction of the erosive winds. Supporting evidence

comes from the southern part of the Lower LTYu where bedding planes dip southeast (N134°; Fig. 6) and appear to control yardang transversal asymmetry: the smooth, gentle faces of the individual yardangs fit bed dips whereas the steep faces represent bed strike sections. Elongations of the yardangs crests were in turn likely generated by superimposed, westerly winds blowing in N67° and N83° directions (Fig. 4A). HiRISE images that cover the transversally-symmetrical yardang forms of the upper LTY subunits (Fig. 2C, D, E) suggest subhorizontal, more gently dipping internal bounding surfaces, such as expressed in our cross-section (Fig. 8A).

Beyond the morphology of the yardang shapes, there are clear differences in how the units have weathered. The lower and middle units appear as cliff -forming units suggesting a substrate prone to fractures (Fig. 2). The upper units show less of this type of failure with many yardangs tailing off rather than failing in abrupt cliffs. This difference could be reflective of distinct degrees of induration of the material prior to weathering.

Our model for the yardang formation is that the general elongation of the yardang forms is controlled by the prevailing erosive wind direction whereas the transversal profiles of the individual forms are influenced by the internal bedding geometry and, possibly, by the degree of induration of the deposits. This model implies that the Lower LTY subunit - latitudinal dominant direction, and the upper LTY subunits group - meridian dominant direction, must have been shaped by very distinct wind regimes.

To summarize, the stratigraphic LTYu of Mt Sharp is viewed, based on the analysis of the stratal architectures, to be an amalgamated stack of at least two, possibly four, ancient erg systems. From the analysis of the surface textures, the morphological elements are inferred to be yardangs (i.e., forms been generated by wind erosion). The duration estimated for the deposition of the LTYu including the generation of the basal unconformity, the timing of the yardang formation, and the possible source of the yarding-forming material are discussed below.

6. Discussion

6.1. The role of water in the deposition/preservation of the LTYu

The purpose of the following discussion is to assess the potential influence of regional moisture in the accumulation and preservation of the LTYu's ergs.

There is no direct evidence of the influence of surface or subsurface water on the accumulation of the eolian material of the LTYu. This does not mean there was not, because as noted above, potential indications of wet interdunes might be too subtle to be seen in available imagery. Conversely, we note that the presence of free surface water, or water as capillary fringe in the subsurface, is not a limiting condition for erg deposits to accumulate. Marzolf (1988) acknowledged that a well-drained, low-relief surface is an important enhancing factor for erg development, and that fluvial processes only lead to significant concentration of sand that is subsequently deflated into erg dunes. On Mars, one could expect that total sediment yield increase monotonically with surface runoff, because there is no moisture-related, vegetation cover to reduce runoff. Additionally excessive runoff reduces the ability for wind to deflate the surface due to sand stabilization by water saturation in the initial sand accumulation. Conversely, a prolonged arid period where fresh alluvium is not generated, could favor formation of desert pavement, which limits surface wind deflation (Marzolf, 1988).

Additional indirect information about the presence of water comes from the preservation itself of erg deposits between the sub-unconformities (i.e., supersurfaces). The thickness of the deposits left by an erg in the rock record is both a function of deposition and subsequent removal of these deposits during supersurface formation. The extent of erg-sediment removal during supersurface development is governed by: (1) deflation to the water table; (2) deflation to a point where a protective armored lag occurs; (3) development of a protective mantle of vegetation; or (4) the time interval before deposition by ergs or other depositional systems (e.g., alluvial fan) resumes (Kocurek, 1988). These reasons are not mutually exclusive. With respect to our study, points 1) and 2) are sound possibilities but certainly not unique processes since the supersurfaces of the LTYu are not planar and horizontal (Fig. 8A). Point 4 is related to the migration of sand seas by changing wind patterns due to changes in the arrangement of the Wilson's nodes (Wilson, 1971). In ergs, sand is deflated from and/or transported across areas of

accelerating or diverging winds, areas referred to as "node of attachment", to accumulate in areas of converging and/or decelerating flow, referred to as "nodes of separation". We consider point 4 to be the most likely in that: (i) the LTYu itself is overlain by the Benched unit, another erg system (Anderson et al., 2018); (ii) LTYu sub-unconformities have an apparent limited lateral extent and are intersecting each other (Fig. 8A).

The development and the preservation of erg deposits of the LTYu point to the existence of a temporally equivalent and geographically adjacent alluvial system where fluvial deposits were deflated to provide a source of particles that were entrained to form eolian dunes, and from which water table high stands driving preservation of eolian deposits might have been sustained. Considering the observed dominant paleo sand transport direction towards the center of Gale crater (Fig. 6), an intuitive location for the alluvial system development would be the interior flank of the NW crater rim. The stratigraphic elevation range of the LTYu that is ca -3.3 to -1.9 km is consistent with the modern northern rim elevation of -2.46 km (Irwin et al., 2005) given the facts that the northern rim originally may have been slightly higher and that we have observed that eolian deposits are composed of bedforms climbing up the central mound.

If we admit the existence of an alluvial system that was deflated to feed eolian dunes, we are still left with the question of the ultimate source of this material. The geographic proximity, the similarity of the bright tone, and the textural comparison of the LTYu with the MFF have led some authors (e.g., Zimbelman & Griffin, 2010; Tanaka et al., 2014) to consider the LTYu as an isolated remnant of the regional widespread MFF. While the primary depositional mechanism(s) of the MFF remains uncertain, volcanic airfall, ignimbrites, or eolian dust are leading hypotheses (e.g., Mandt et al., 2008). Whatever its origin, it is clear that intermittent (Di Pietro et al., 2018) and subsequent (Burr et al., 2009) reworkings by fluvial systems of the MFF primary deposits have occurred. The final view that the eolian systems of the LTYu are recycled deposits of the MFF is consistent with the recent findings that a significant part of the MFF may have been deposited during the Hesperian (Kerber & Head, 2010; Zimbelman & Scheidt, 2012).

6.2. Timing and duration of the LTYu deposition

The LTYu marks the resumption of sediment accumulation above a major hiatal stratigraphic contact that is the basal unconformity. The presence of an exhumed crater (Fig. 3C) and paleo-yardang forms buried by the basal LTYu deposits indicate that the underlying dark-toned layers of the Syu1 became lithified enough to retain craters and be partially eroded before the lighter unit deposition. While a consolidation of sediments entails a certain period, the question is how much time actually is collapsed within this contact?

The partly exhumed crater currently is a poorly rounded, very shallow pit ~600 meters in diameter and a few meters deep (Fig. 3C). It is a fairly planar feature which does not show a real rim, suggesting it has been planed off prior to the LTYu deposition. A power law (Garvin et al., 2003) between the martian crater depths and diameters predicts this crater must have had an initial depth ranging in between 10 and 20 meters, so that it can be inferred that its rim has been eroded by a few tens of meters. Using crater obliteration rates of about 1 m/My for the Hesperian - Amazonian (Quantin-Nataf et al., 2019), the aerial exposure time of the crater retention surface, after impact, must have been in the range of one to a few tens of million years.

An another way of evaluating how long the top surface of the Syu1 has been exposed is to calculate the lapse-time required for the surface to have a significant chance of having been impacted, at the Early-Late Hesperian age (i.e. 3.4 Gy) by a bolide able to generate a 600 m wide crater. The calculation is based on the crater size frequency distribution from Hartmann (2005) and the crater production function from Neukum et al. (2001). If we take as a boundary condition that the exposed surface was about 2,000 km^2 (assessed original extent of the exposed surface), 70 km^2 (current extent of the LTYu), 14 km^2 (current extent of the visible contact surface), the computed recurrences times are about 14, 400, and 2,000 Myrs, respectively. This tentative calculation that yields a range of over two orders of magnitude is not very relevant by itself. It only shows that it is consistent with the above inference of an aerial exposure duration of at least few tens of million years.

As to how long the net accumulation of the entire exposed LTYu itself took, it can be approximated as several tens of million years, based on the terrestrial analog from southern Utah. According to Blakey et al. (1996), the major stratigraphic erg system in this region enclosing two deflationary supersurfaces initiated in the Early Jurassic and terminated in the Middle Jurassic, spanning a time interval of about 20 Myrs. It should be added that a time-interval of 20 M. earth years does not necessarily conflict with a possible control of erosion-deposition cycles by the variation of Mars' orbital parameters. For example, it has been shown for the past 10 M. earth years on Mars that the period of high-mean obliquity is 4 Myrs at least (Laskar et al., 2004), so that each LTYu subunit might have been deposited during a period of high obliquity.

6.3. Timing of the yardang formation

The apparent lack of craters on the surface of the light-toned yardang-forming material itself may suggest that the development of the yardang forms is quite recent (Anderson & Bell, 2010). However, Le Deit et al. (2013; fig. 13b) have shown that yardang forms of the LTYu are buried by a set of continuous, planar strata of the Syu2. Another argument for an early development of the LTYu yardang forms comes from the observation that the overlying and more recent units (i.e., Syu2 and Bu) do not exhibit yardangs. Similarly, if we accept that the yardang long axes are subparallel to the prevailing wind directions, then it is difficult to reconcile the nearly orthogonal change of the wind prevailing directions between the Lower LTY subunit and the upper LTY subunits (Fig. 2) with deflection of a single dominant wind over such a short spatial scale. Moreover, neither of the two prevailing directions (i.e., East-West and North to South respectively) is consistent with recent, Mt Sharp related, up- or downslope-wind.

These observations rather suggest that at least two distinct yardang-generating wind episodes occurred during the initial development of Mt Sharp, and not after Mt Sharp formed. Our interpretation for the LTYu is that a package of eolian sand was deposited over an erosional surface of yardangs eroded into the previous package of indurated material. This repeated to form at least two (2), possibly four (4),

apparent sequences involving eolian sand deposition, induration to some degree, and erosion to create yardangs. It is thought that the LTYu was deposited, partially lithified, and eroded into yardangs cyclically. The successive burial-related induration of the yardangs have likely made them difficult to obliterable, so that recent degradation must have been respective of their original form. Incomplete lateral burial of the Lower LTY subunit would have caused the superimposition of several yardang directions over it.

Such a type of deposition-erosion sequence has been documented on Mars in the MFF of the Amazonis Planitia Region (Wells & Zimbelman, 1989; Mandt et al., 2009). In that area, two sets of yardangs were formed by winds of nearly orthogonal directions. An older set of yardangs was buried by a deposit 100 m in thickness, and later exposed by the easterly winds that formed the younger yardangs. Similarly, Chojnacki et al. (2020) have reported in Valles Marineris, atop Hesperian-aged layered deposits, a lithified field of paleo-barchan dunes that climbed up onto the flanks of an eroded sedimentary mound, before being lithified.

Finally, it should be noted that lithified yardang forms apparently exist in the Earth's stratigraphic record. An example comes from the Canyonlands National Park, SE Utah where partly exhumed, aligned sandstone ridges occur at the upper unconformable surface of the Lower Permian (Leonardian), and are onlapped by the Lower Triassic (Tewes & Loope, 1992). The potential time gap that here corresponds to the paleo-yardangs is of the magnitude of 20 Myrs.

7. Conclusion: Atmospheric conditions in Gale crater in the Late Hesperian

The eolian material of the LTYu was deposited in a context of regional aridity. However the putative cycles of eolian deposition – and (partial) erosion which compose the LTYu are believed to reflect change in the regional moisture budget, swinging from semi-arid (deposition) to arid (erosion) conditions. Assuming that alluvial fans are the original sources of sands, it is expected that: (i) a decreasing fluvial flow-recurrence interval, as a result of increasing moisture, will increase sand

deflation availability and raise erg water table levels, favoring accumulation and preservation of ergs respectively; (ii) conversely, increased aridity will cause a dwindling of sand supplied to ergs and favor development of yardangs and erosional bounding supersurfaces. We have also seen that the generation of bounding supersurfaces might be influenced by the migration of sand seas due to changes in the arrangement of the Wilson's nodes. Given the high probability of quasi-static physiographic conditions in Gale crater, a change of Wilson's nodes implies a regional change of wind regime.

Our final view is that cyclic aridity changes must have been coupled in climatic cycles with changes in wind regimes to generate the sequences of eolian erosion-deposition recorded by the LTYu. We further propose that the major unconformities (i.e., basal and top LTYu unconformities) have primarily been associated with severe and prolonged aridity whereas sub-unconformities within the LTYu have primary been related to wind regime changes. Whether these putative climatic cycles recorded in Gale crater are global and periodic, and so related to the variations in orbital and spin axis parameters of the planet, cannot be resolved at this time. At any rate, what can be highlighted here is that the regional unconformity that separates the Lower and Upper mound formations of Mt Sharp, and the subsequent emplacement of the LTYu, together express a clear tendency toward more arid environments for that region of Mars around the Early – Late Hesperian transition. Given the large time scale that is involved (i.e., a few tens of million years at least) we consider it likely that the local evidence for increased aridity in the Mt Sharp stratigraphy is part of a climate change affecting the whole planet.

Acknowledgments

The authors gratefully acknowledge support from the NASA Mars Science Laboratory Mission and the efforts of the MSL engineering and science operations teams. This work was supported in France by the Centre National des Etudes Spatiales (CNES) and the Centre National de la Recherche Scientifique (CNRS). G. Dromart, L. Le Deit, C. Quantin-Nataf, N. Mangold, and D. Rubin thank Fondation des Treilles for support for a meeting during which they had the opportunity to discuss about eolian sedimentation on Mars. Gratitude is due to R. Anderson, L. Edgar, and K. Herkenhoff (USGS) for

discussions that helped improve this work. Thanks to Drs. Kenneth Edgett (Malin Space Center) and Robert Sullivan (Cornell) for their very valuable feedback on an early version of the manuscript, and to anonymous reviewers for their constructive comments.

Figure Captions

Fig.1: (A) CTX mosaic of Gale crater; Fig1B indicated by light pink box. (B) Inset showing key geological units, including in a stratigraphic ascending order the Small yardang unit 1 (Syu1), Light-Toned Yardang unit (LTYu), Small yardang unit 2 (Syu2), and Benched unit (Bu), and major unconformities that bound these units; white dot is the rover location from which the LD RMI view of (C) was shot, and white dashed bars delineate the field of view of (C). (C) Long-Distance Remote Micro Imager mosaic (ChemCam instrument onboard Curiosity Rover) showing: (i) the strong rock tone contrast between the Syu1 (yielding polyhydrated sulfate spectral signatures) and the LTYu (no spectral signature detected); (ii) the clear sub-horizontal layering in Syu1 (foreground) compared to the confusing situation in the LTYu (background) where, in most of the exposure, there are no clear layers in the RMI mosaic.

Fig.2: Morphometric attributes of the Light-Toned Yardang unit from orbit. (A) Measurements of the LTYu's attitudes. Length, width, aspect ratio, and direction of individual ridges form were measured manually using *Adobe Illustrator*® software (metrics are provided in SM_Table 1). Colored bars represent the ridge crest-lines. Insets are rose diagrams of measured crest-line directions. We restricted our measurements to unmistakable yardang forms, the length of which is >30 m, due to a too possible inaccurate measurement of the small features. (B, C, D, E) Distinctive morphological types of ridge forms of the Middle, Upper, Top LTYu subunits respectively (B: HiRISE image ESP_030102_1750; C, D: HiRISE image ESP_030880_1750; E: ESP_031803_1750). Dashed lines (C, D, E) highlight yardang contours.

Fig. 3: Contact between the LTYu and the Syu1. (A) Geometric measurements of the unconformity that bounds the overlying LTYu and the underlying Syu1. (B) Close-up of HiRISE image ESP_028269_1750 (36.7 cm/pixel; 110 cm across resolved) showing that long axes of the yardang's crest lines (dashed lines) of the upper Syu1 and lower LTYu are oriented differently. This provides evidence that the Syu1 yardang forms developed prior to LTyu deposition indicating the unconformity

555 encompasses a long time interval. (C) Close-up of HiRISE image ESP_019698_1750 (29.1 cm/pixel;
556 87 cm across resolved) showing that now the partially-exhumed crater at the contact had been stripped
557 off and partially filled prior to the deposition of the LTYu.
558
559 Fig. 4: Orbital and ground views of the Lower LTY subunit. (A) HiRISE stereo terrain model showing
560 the texture detail of the yardang surface. Yardangs are elongated and transversally asymmetric forms.
561 The general stepped pattern results from the intersection of two linear trends (i.e. N67° and N83°). The
562 light-green, red and blue colored areas represent the ground projection (i.e., view shed) of the LD RMI
563 mosaic below. Cross-hatching indicates viewshed is outside of HiRISE stereo terrain model, and
564 therefore reduced to MOLA terrain model. (B) Mosaic of five LD RMI images (CCAM06251) taken
565 on sol 1183 at a distance of 6.9 km. The blue- and red-colored stripes are virtual projections transposed
566 onto HiRISE image A. N53° is the general strike direction of the slope. (C) LD RMI mosaic showing a
567 strike view of the beds (marked with red lines). The individual yardang forms are made up of evenly
568 distributed, subparallel and planar beds that dip away towards southeast (apparent dip of [4-12]°). The
569 general orientation of the yardang crests (black lines) is N67°, oblique to that of the slope.
570
571 Fig. 5: Close-up of CCAM06251 showing bedding geometries of the Lower LTYu. Most of the
572 observations in this area indicate a bedding orientation that dips away, with limited variation, in an
573 opposite direction to the local slope (i.e. southeast against northwest) so that bed strike sections actually
574 were traced. Bed traces (white lines) are extensive (i.e., several tens of meters long), and are mostly
575 planar and parallel. Only a few and minor local angular unconformities are traceable. Individual,
576 resistant yardang forms, which seem to be uniformly distributed down the general slope, show sets of
577 evenly stacked, thickening- and possibly steepening-upward beds.
578
579 Fig. 6: Lower LTY subunit. Mapped bed traces intersecting the land surface (red lines) over the HiRISE
580 stereo terrain model derived from full-resolution HiRISE images PSP_009149_1750 (27.7 cm/pixel; 83
581 cm across are resolved) paired with PSP_009294_1750. The light-green colored areas represent the
582 ground projection (i.e., view shed) of the LD RMI mosaic of Fig. 4A. The bed traces show a parallel,

583 linear to curvilinear pattern, suggesting planar geometry, with an apparent fairly uniform spacing. The
584 strike azimuth of the bed traces is quasi steady, and range between N31° and N55° directions (indicated
585 strike azimuths are general directions of local, bed trace clusters). The average dip is towards southeast
586 (i.e., N134°). Bedding planes are coincident with the local topography at some places. The dip
587 magnitude of these surfaces were not measurable because of their very limited extension. The dominant
588 wind direction is assumed reflective of the dominant direction of the sediment transport.
589
590 Fig. 7: Unscaled mechanical model that explains how the bed sets of the Lower LTY subunit were
591 deposited and preserved by winds dominantly blowing towards southeast, and then eroded by wind the
592 direction of which was approximately orthogonal to the dominant "depositional" wind.
593
594 Fig.8: Stratigraphic models for the Light-Toned Yardang unit. (A) Tentative stratigraphic cross section
595 of the LTYu, in context. The geometry of the major unconformity at the base of the LTYu suggests the
596 presence of an early moat around Mt Sharp, as predicted by Kite et al., 2016. The cross-section clearly
597 shows that the LTYu formed from climbing dunes on the side of a preexisting mound. Contact
598 geometries in between morphostratigraphic units of the LTYu are not certain, and there is no available
599 rover imaging from the surface perspective to constrain the stratal organization of the Middle to Top
600 LTY subunits (i.e., no LD RMI). In contrast to climbing bounding surfaces of the Lower LTY subunit,
601 internal bounding surfaces of the Middle to Top LTY subunits are difficult to discern at best (see
602 SM_Fig. 4) and drawn as subhorizontal, more gently dipping surfaces. (B) Tentative chronostratigraphic
603 chart (i.e., Wheeler Diagram) for the multistory deposition/erosion of the LTYu. Grey-shaded areas
604 express periods of deposition. Blank areas represent periods of non-deposition / erosion.

605 **References**

606

607 Anderson, R.B., Bell III, J.F., 2010. Geologic mapping and characterization of Gale Crater and
608 implications for its potential as a Mars Science Laboratory landing site. Mars J. 5, 76–128.
609 http://dx.doi.org/10.1555/mars.2010.0004.

610 Anderson, R.B., Edgar, L.A., Rubin, D.M., Lewis, K.W., Newman C., 2018. Complex bedding
611 geometry in the upper portion of Aeolis Mons, Gale crater, Mars. Icarus 314, 246-264.
612 https://doi.org/10.1016/j.icarus.2018.06.009

613 Blakey, R.C., Peterson, F., Kocurek, G., 1988. Synthesis of late Paleozoic and Mesozoic eolian deposits
614 of the Western Interior of the United States. Sed. Geol. 56, 3-127. https://doi.org/10.1016/0037-
615 0738(88)90050-4.

616 Blakey, R.C., Jones, L.S., Havholm, K.G., 1996. Stratigraphic Analysis of Eolian Interactions with
617 Marine and Fluvial Deposits, Middle Jurassic Page Sandstone and Carmel Formation, Colorado Plateau,
618 U.S.A. J. Sed. Res. 66, 324-342. https://doi.org/10.1306/D426833D-2B26-11D7-8648000102C1865D.

619 Bridges, N.T., Banks, M.E., Beyer, R.A., Chuang, F.C, Noe Dobrea, E.Z., Herkenhoff, K.E., Keszthelyi,
620 L.P., Fishbaugh, K.E., McEwen, A.S., Michael, T.I., Thomson, B.J., Wray, J.J., 2010. Aeolian
621 bedforms, yardangs, and indurated surfaces in the Tharsis Montes as seen by the HiRISE camera:
622 evidence for dust aggregate. Icarus 205, 165-182. http://dx.doi.org/10.1016/j.icarus.2009.05.017.

623 Brookfield, M.E., 1992. Eolian systems, in: Walker, R.G., James, N.P. (Eds) Facies Models: response
624 to sea level change. Geol. Ass. Canada, Memorial Univ. of Newfoundland, pp.143-156.

625 Burr, D.M., Enga, M-T., Williams, R.M.E., Zimbelman, J.R., Howard, A.D., Brennand, T.A., 2009.
626 Pervasive aqueous paleoflow features in the Aeolis/Zephyria Plana region, Mars. Icarus, 200, 52–76.
627 https://doi.org/10.1016/j.icarus.2008.10.014.
628
629 Chojnacki, M., Fenton, L.K ., Weintraub, A.R., Edgar, L.A., Jodhpurkar, M.J., Edwards, M.S., 2020.
630 Ancient Martian Aeolian Sand Dune Deposits Recorded in the Stratigraphy of Valles Marineris and
631 Implications for Past Climates. J. Geophys. Res.: Planets 125, 9. https://doi.org/10.1029/2020JE006510.
632
633 Di Pietro, I., Ori, G.G., Pondrelli, M., Francesco Salese, F., 2018. Geology of Aeolis Dorsa alluvial
634 sedimentary basin, Mars. J. of Maps, 14:2, 212-218. https://doi.org/10.1080/17445647.2018.1454350.
635

636 El-Baz, F., Breed, C.S., Grolier, M.J., McCauley, J.F. 1979. Eolian features in the western desert of
637 Egypt and some applications to Mars. J. Geophys. Res.: Solid Earth 84, 8205-8221.
638 https://doi.org/10.1029/JB084iB14p08205.
639
640 Fraeman, A.A., Ehlmann, B.L., Arvidson, R.E., Edwards, C.S., Grotzinger, J.P., Milliken, R.E., Quinn,
641 D.P., Rice, M.S., 2016. The stratigraphy and evolution of lower Mount Sharp from spectral,
642 morphological, and thermophysical orbital data sets. J. Geophys. Res.: Planets 121, 1713–1736.
643 https://doi.org/10.1002/2016JE005095.

644 Garvin, J.B., Sakimoto, S.E.H., Frawley, J.J., 2003. Craters on Mars: geometric properties from gridded
645 MOLA topography, Abstract 3277, in: Proceedings of the Sixth International Conference on Mars.
646 Pasadena, California. California Institute of Technology 20–25 July.

647 Grotzinger, J.P., Milliken, R.E., 2012. The Sedimentary Rock Record of Mars: Distribution, Origins,
648 and Global Stratigraphy, in: Grotzinger, J.P. & Milliken R.E. (Eds), Sedimentary Geology of Mars.
649 S.E.P.M. Spec. Publ. 12, pp. 1-48.

650 Grotzinger, J.P., Gupta, S., Malin, M.C., M.C., Rubin, D.M., Schieber, J., Siebach, K., Sumner, D.Y.,
651 Stack, K.M., Vasavada, A.R., Arvidson, R.E., Calef, F., Edgar, L., Fischer, W.F., Grant, J.A., Griffes,
652 J., Kah, L.C., Lamb, M.P., Lewis, K.W., Mangold, N., Minitti, M.E., Palucis, M., Rice, M., Williams,
653 R.M.E., Yingst, R.A., Blake, D., Blaney, D., Conrad, P., Crisp, J., Dietrich, W.E., Dromart, G., Edgett,
654 K.S., Ewing, R.C., Gellert, R., Hurowitz, J.A., Kocurek, G., Mahaffy, P., McBride, M.J., McLennan,
655 S.M., Mischna, M., Ming, D., Milliken, R., Newsom, H., Oehler, D., Parker, T.J., Vaniman, D., Wiens,
656 R.C., Wilson, S.A., 2015. Deposition, exhumation, and paleoclimate of an ancient lake deposit, Gale
657 crater, Mars. Science 350, aac7575. http://dx.doi.org/10.1126/science.aac7575.

658 Hartmann, W.K., 2005. Martian cratering 8: isochron refinement and the chronology of Mars.
659 Icarus 174, 294-320. https://dx.doi.org/10.1016/j.icarus.2004.11.023

660 Irmen, A.P., Vondra, C.F., 2000. Aeolian sediments in lower to middle Triassic rocks of central
661 Wyoming. Sed. Geol. 132, 69-88. https://doi.org/10.1016/S0037-0738(99)00129-3.

Irwin, R.P., Howard, A.D., Craddock R.A., Moore, J.M. 2005. An intense terminal epoch of widespread fluvial activity on early Mars: 2. Increased runoff and paleolake development, J. Geophys. Res. 110, E12S15, doi:10.1029/2005JE002460.

Kirk, R.L., Howington-Kraus, E., Rosiek, M.R., Anderson, J.A., Archinal, B.A., Becker, K.J., Cook, D.A., Galuszka, D.M., Geissler, P.E., Hare, T.M., Holmberg, I. M., Keszthelyi, L.P. Redding, B.L. Delamere, W. A., Gallagher, D., Chapel, J.D., Eliason, E.M., King, R., McEwen, A.S., 2008. Ultrahigh resolution topographic mapping of Mars with MRO HiRISE stereo images: Meter-scale slopes of candidate Phoenix landing sites. J. Geophys. Res. 113, E12. https://doi.org/10.1029/ 2007JE003000.

Kite, E.S., Lewis, K.W., Lamb, M.P., Newman, C.E., Richardson, M.I. 2013. Growth and form of the mound in Gale Crater, Mars: Slope wind enhanced erosion and transport. Geology 41, 543–546. https://doi.org/10.1130/g33909.1.

Kite, E.S., Sneed, J., Mayer, D.P., Lewis, K.W., Michaels, T.I., Hore, A., Rafkin, S.C.R 2016. Evolution of major sedimentary mounds on Mars: Buildup via anticompensational stacking modulated by climate change. J. Geophys. Res.: Planets 121, 2282–2324. https://doi.org/10.1002/2016JE005135.

Kneissl, T., van Gasselt, S., Neukum, G. 2010. Measurement of strike and dip of geologic layers from remote sensing data: New software tool for ArcGIS. Lunar and Planetary Science Conference, 41, 1640.

Kocurek, G. 1986. Origins of low-angle stratification in eolian deposits, in: Nickling, W.G. (Ed.), 16th Annual Binghamton Geomorphology Symp. Allen and Unwin, London, pp. 177-193.

Kocurek, G., 1988. First-order and super bounding surfaces in eolian sequences – bounding surfaces revisited. Sed. Geol. 56, 193-206. https://doi.org/10.1016/0037-0738(88)90054-1.

Laity, J.E., 2011. Wind erosion in drylands, in: Thomas, D.S.G. (Ed.), Arid zone geomorphology: Process, form and change in drylands (3rd ed.). New York, NJ: John Wiley, pp. 539–568.

685 Laskar, J., Correia, A.C.M., Gastineau, M., Joutel, F., Levrard, B., 2004. Long term evolution and
686 chaotic diffusion of the insolation quantities of Mars. Icarus 170, 343–364.
687 https://doi.org/10.1016/j.icarus.2004.04.005.

688 Le Deit, L., Hauber, E., Fueten, F., Pondrelli, M., Rossi, A.P., Jaumann, R., 2013. Sequence of infilling
689 events in Gale Crater, Mars: Results from morphology, stratigraphy, and mineralogy. J. Geophys. Res.:
690 Planets 118, 2439–2473. https://doi.org/10.1002/ 2012je004322.

691 Le Mouélic, S., Gasnault, O., Herkenhoff, K.E., Bridges, N.T., Langevin, Y., Mangold, N., Maurice,
692 S., Wiens, R.C., Pinet, P., Newsom H.E., Deen R.G., Bell, J.F., Johnson, J.R., Rapin, W., Barraclough,
693 B., Blaney, D.L., Deflores, L., Maki, J., Malin, M.C., Pérez, R., Saccoccio, M., 2015. *The ChemCam*
694 *Remote Micro-Imager at Gale crater: Review of the first year of operations on Mars*. Icarus 249, 93-
695 107. https://doi.org/10.1016/j.icarus.2014.05.030.
696
697 Malin, M.C., Edgett K.S., 2000. Sedimentary Rocks of Early Mars. Science 290, 1927–1937.
698 https://dx.doi.org/10.1126/science.290.5498.1927.
699
700 Mandt, K.E., de Silva, S.L., Zimbelman, J.R., Crown, D.A., 2008. Origin of the Medusae Fossae
701 Formation, Mars: Insights from a synoptic approach. J. Geophys. Res. 113, E12011.
702 https://doi.org/10.1029/2008JE003076.
703
704 Mandt, K.E., de Silva, S.L., Zimbelman, J.R., Wyrick, D., 2009. Distinct erosional progressions in the
705 Medusae Fossae formation, Mars, indicate contrasting environmental conditions. Icarus 204, 471–477.
706 https://doi.org/10.1016/j.icarus.2009.06.031.

707 Marzolf, J.E., 1988. Controls on late Paleozoic and early Mesozoic eolian deposition of the western
708 United States. Sed. Geol. 56, 167-191. https://doi.org/10.1016/0037-0738(88)90053-X.

709 McCauley, J.F., 1973. Mariner 9 evidence for wind erosion in the equatorial and mid-latitude regions of
710 Mars. J. Geophys. Res. 78, 4123-4137. https://doi.org/10.1029/JB078i020p04123.

McCauley, J.F., Grolier, M.J., Breed C.S., 1977. Yardangs, in Doehring, D.O. (Ed.), Geomorphology in Arid Regions. Allen and Unwin, Boston (USA), pp. 233–269.

Milliken R.E, Grotzinger, J.P., Thomson, B.J., 2010. Paleoclimate of Mars as captured by the stratigraphic record in Gale Crater. Geophys. Res. Lett. 37, L04201. https://doi.org/10.1029/2009GL041870.

Neukum, G., Ivanov B.A., Hartmann W.K., 2001. Cratering records in the inner solar system in relation to the lunar reference system Space Sci. Rev. 96, 1-4, 55-86. https://doi:10.1023/A:1011989004263.

Peret L., Gasnault O., Dingler R., Langevin Y., Bender S., Blaney D., Clegg S., Clewans C., Delapp D., Donny C., Johnstone S., Little C., Lorigny E., McInroy R., Maurice S., Mittal N., Pavri B., Perez R., Wiens R.C., and Yana C., 2016. Restoration of the autofocus capability of the ChemCam instrument onboard the Curiosity rover. SpaceOps 2016 Conference, (AIAA 2016-2539). https:// doi:10.2514/6.2016-2539.

Quantin-Nataf, C., Craddock, R.A., Dubuffet, F., Lozac'h, L., Martinot, M., 2019. Decline of crater obliteration rates during early martian history. Icarus 317, 427-433. https://doi.org/10.1016/j.icarus.2018.08.005.

Rossi, A.P., Neukum, G., Pondrelli, M., van Gasselt, S., Zegers, T., Hauber, E., Chicarro, A., Foing, B., 2008. Large spring deposits on Mars? J. Geophys. Res.: Planets 113, E08016. https://doi.org/10.1029/2007JE003062.

Scott, D.H., Chapman, M.G. 1995. Geologic and topographic maps of the Elysium Paleolake basin, Mars. U.S. Geol. Surv. Misc. Invest. Ser., MAP I–2397.

Tanaka, K.L., Skinner, J.A., Jr., Dohm, J.M., Irwin, R.P., III, Kolb, E.J., Fortezzo, C.M., Platz, T., Michael, G.G., Hare, T.M., 2014. Geologic map of Mars: U.S. Geological Survey Scientific Investigations Map 3292, scale 1:20,000,000, pamphlet 43 p. https://dx.doi.org/10.3133/sim3292.

Tewes, D.W., Loope, D.B., 1992. Palaeo- yardangs: wind-scoured desert landforms at the Permo-Triassic unconformity. Sedimentology 39, 251-261. https://doi.org/10.1111/j.1365-3091.1992.tb01037.x.

Thomson, B.J., Bridges, N.T., Milliken, R.E., Baldridge, A., Hook, S.J., Crowley, J.K., Marion, G.M., de Souza Filho, C.R., Brown, A.J., Weitz, C.M. 2011. Constraints on the origin and evolution of the layered mound in Gale Crater, Mars using Mars Reconnaissance Orbiter data. Icarus 214, 413–432. https://doi.org/10.1016/j.icarus.2011.05.002

Vasavada, A.R., Grotzinger, J.P., Arvidson, R.E., Calef, F. J., Crisp, J. A., Gupta, S., Hurowitz, J.A., Mangold N., Maurice, S., Schmidt, M.E., Wiens, R.C. Williams, R.M.E., Yingst, R.A., 2014. Over view of the Mars Science Laboratory mission: Bradbury Landing to Yellowknife Bay and beyond. J. Geophys. Res. 19, 1134–1161. https://doi:10.1002/ 2014JE004622.

Ward, A.W., 1979. Yardangs on Mars: Evidence of recent wind erosion. J. Geophys. Res. 84, 8147-8167. https://doi.org/10.1029/JB084iB14p08147.

Wang, J., Xiao, L., Reiss, D., Hiesinger, H., Huang, J., Xu, Y., Zhao, J., Xiao, Z., Komatsu, G., 2008. Geological Features and Evolution of Yardangs in the Qaidam Basin, Tibetan Plateau (NW China): A Terrestrial Analogue for Mars. J. Geophys. Res.: Planets 123, 2336–2364. https://doi.org/10.1029/2018JE005719.

Wells, G.L., Zimbelman, J.R., 1989. Extraterrestrial arid surface processes, in: Thomas, D.S.G. (Ed.), Arid Zone Geomorphology. Belhaven, London, pp. 335–358.

Wilson, I.G., 1971. Desert sandflow basins and a model for the origin of ergs. The Geogr. J. 137, 180-199. https://doi.org/10.2307/1796738.

760 Zhao, N.C., Chenb, J., Hu, C., 2018. Automatic extraction of yardangs using Landsat 8 and UAV
761 images: A case study in the Qaidam Basin, China. Aeolian Research 33, 53-51.
762 https://doi.org/10.1016/j.aeolia.2018.05.002.

763 Zimbelman, J.R., Griffin, L.J., 2010. HiRISE images of yardangs and sinuous ridges in the lower
764 member of the Medusae Fossae Formation, Mars. Icarus 205, 198–210.
765 https://doi.org/10.1016/j.icarus.2009.04.003.

766 Zimbelman, J.R., Scheidt, S.P., 2012. Hesperian age for Western Medusae Fossae Formation, Mars.
767 Science 336 (6089), 1683. http://dx.doi.org/ 10.1126/science.1221094.

Figure

Click here to access/download;Figure;Fig_1_Resubmission.jpg

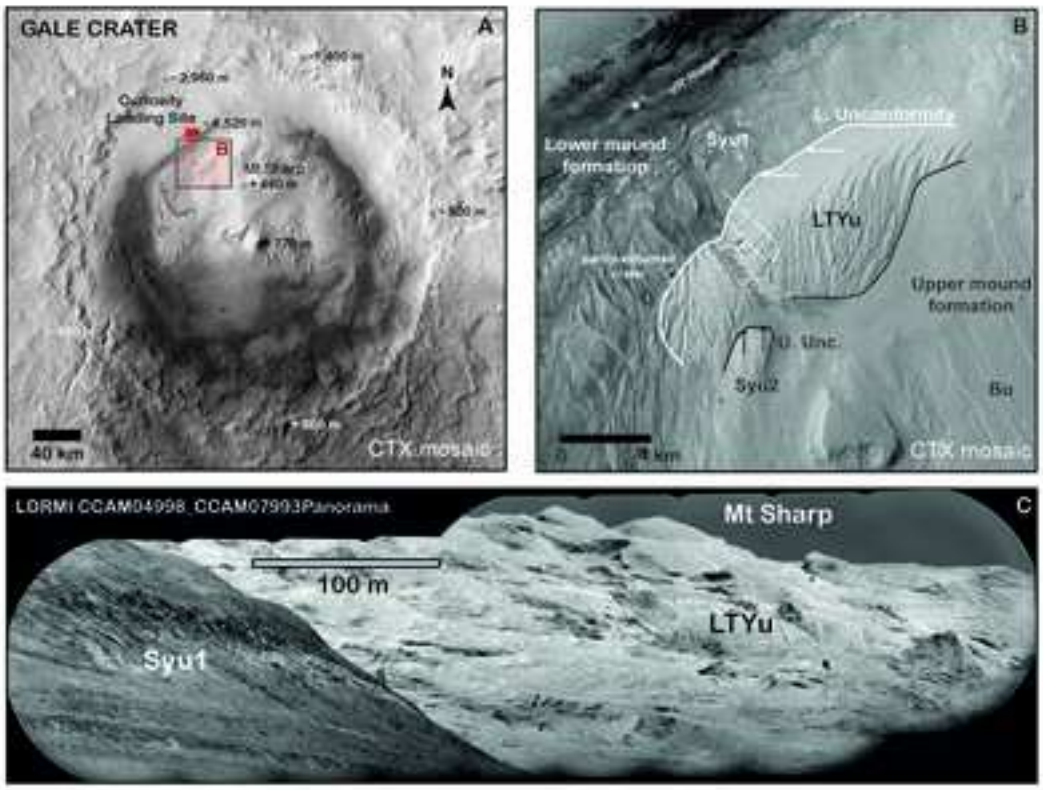

Dromart et al._Fig. 1

Figure

Click here to access/download;Figure;Fig_2__Resubmission.jpg

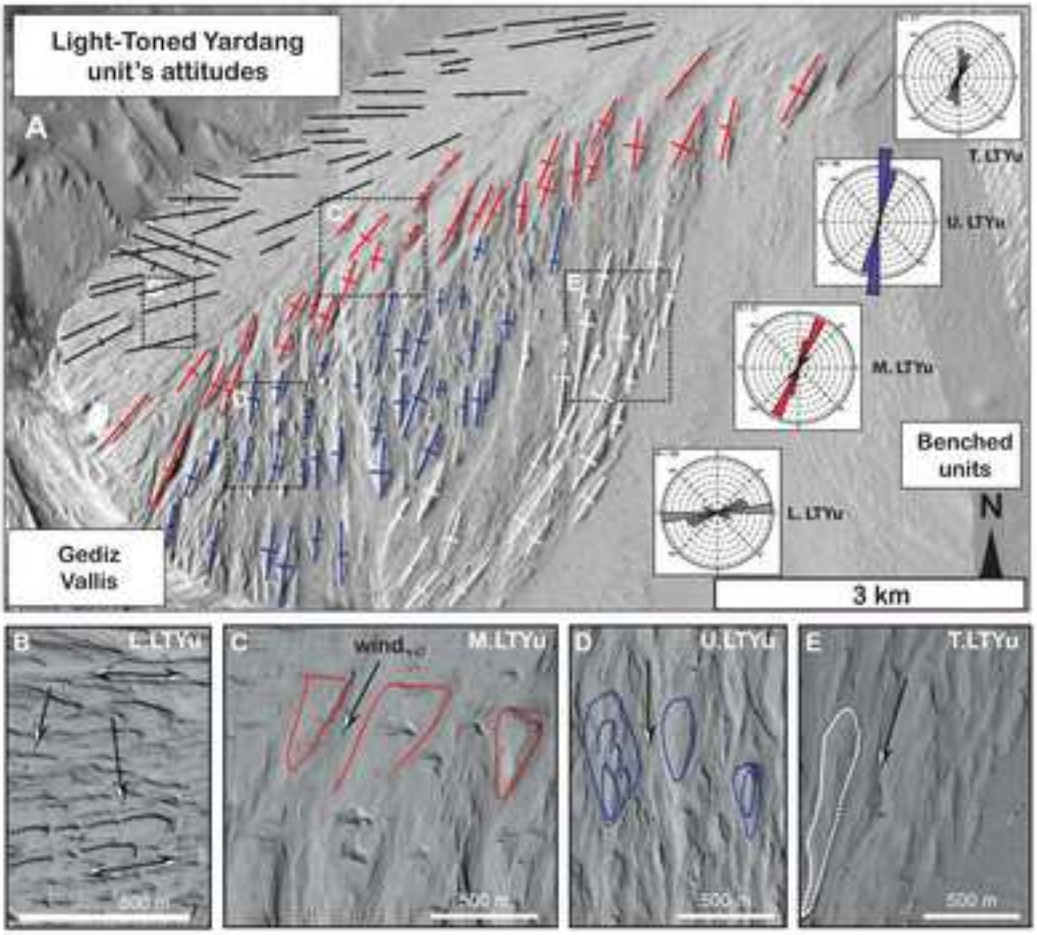

Dromart et al._ Fig. 2

Figure

Click here to access/download;Figure;Fig_3_Resubmission.jpg

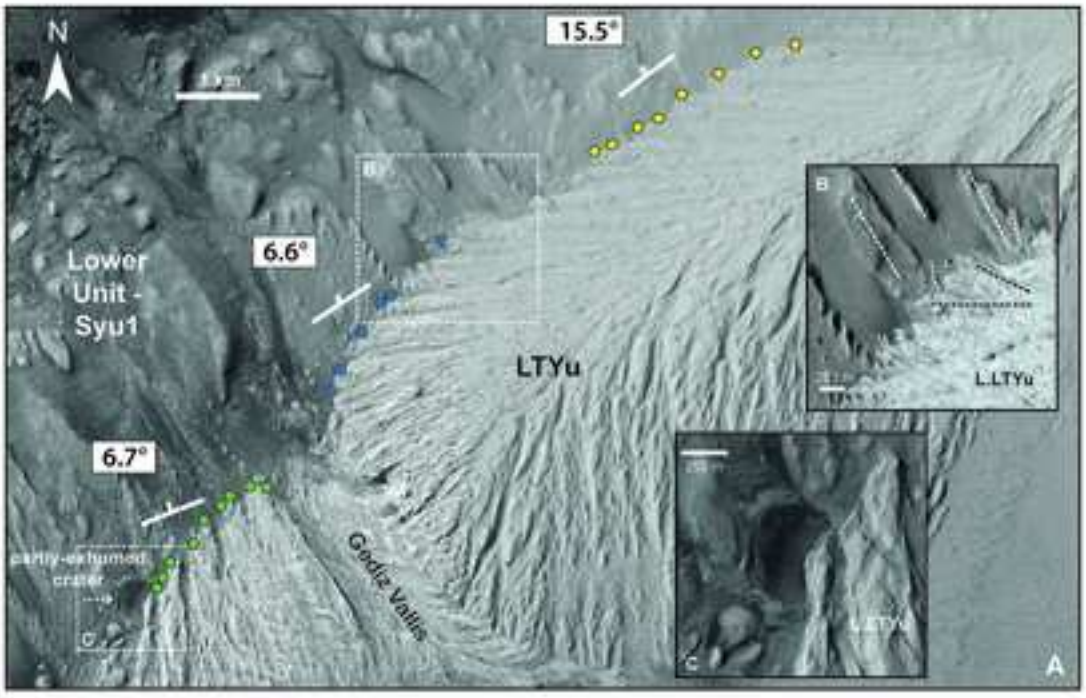

Dromart et al._Fig. 3

Figure

Click here to access/download;Figure;Fig_4_Resubmission.jpg

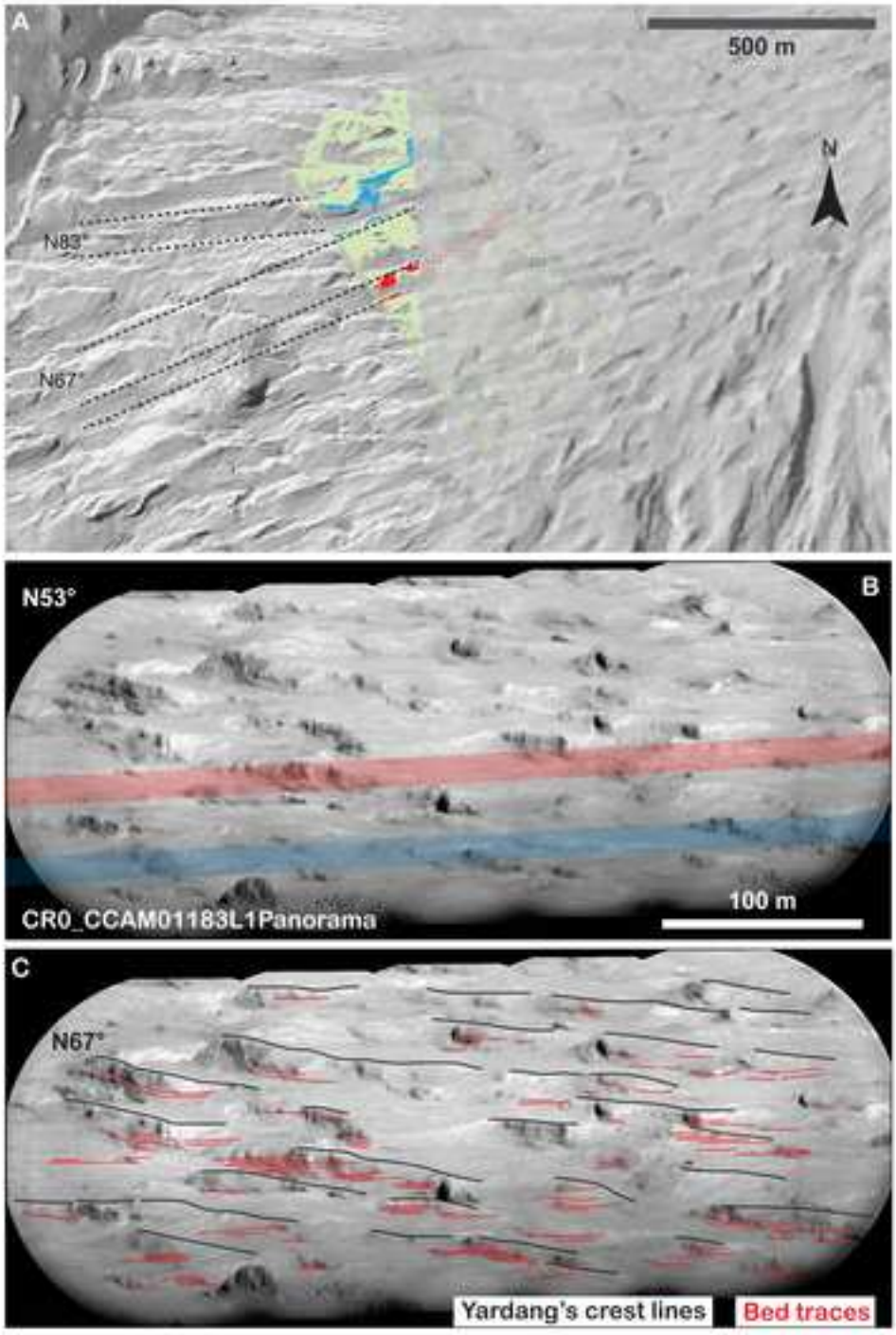

Dromart et al._Fig. 4

Figure

Click here to access/download;Figure;Fig_5_Resubmission.jpg

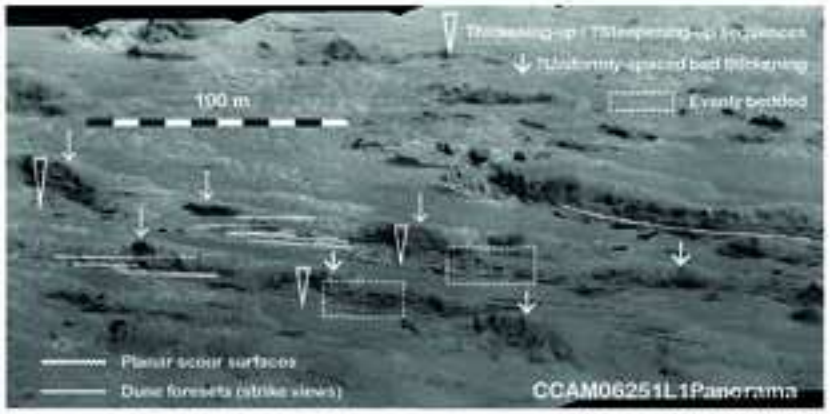

Dromart et al._Fig. 5

Figure

Click here to access/download;Figure;Fig_6__Resubmission.jpg

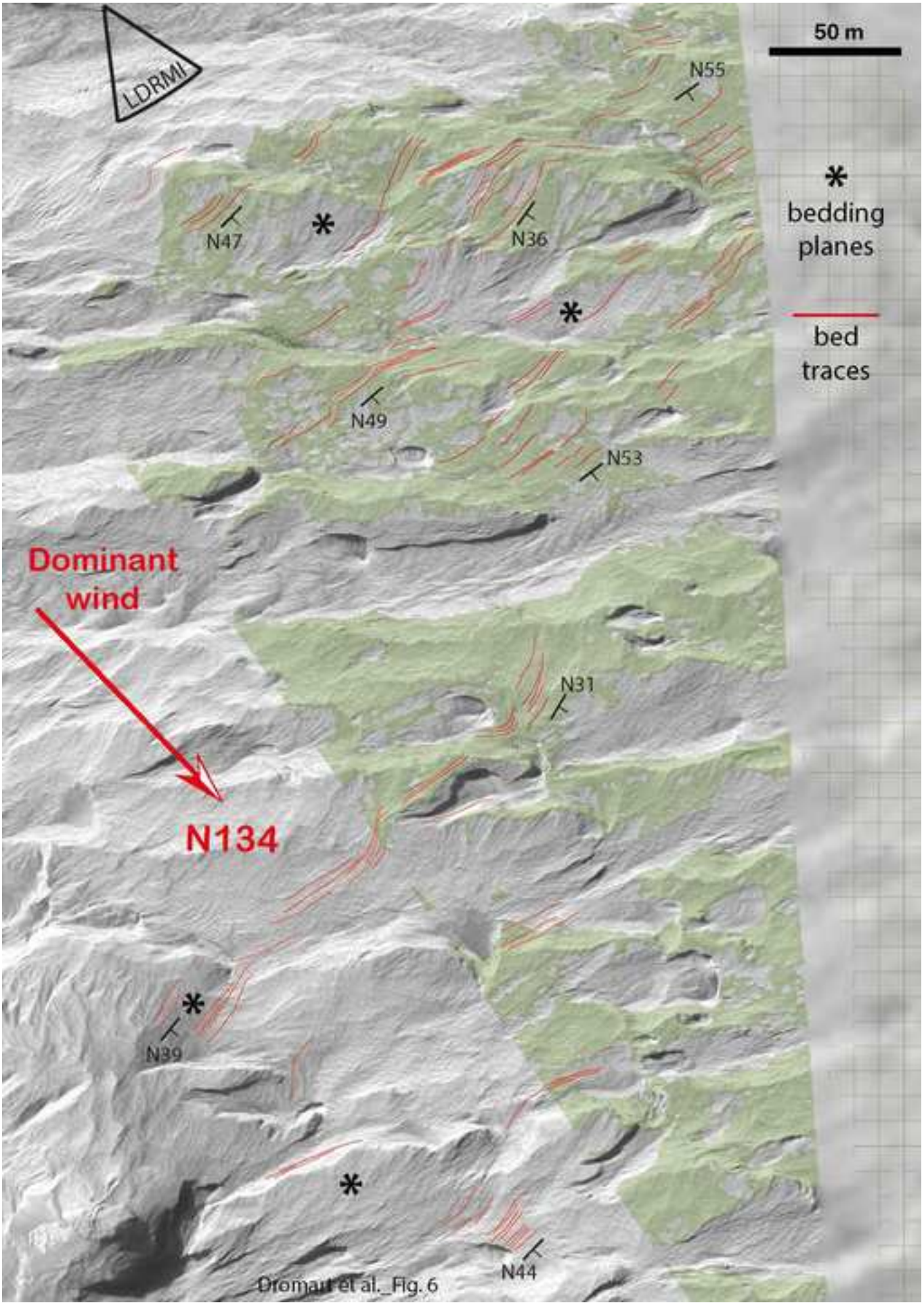

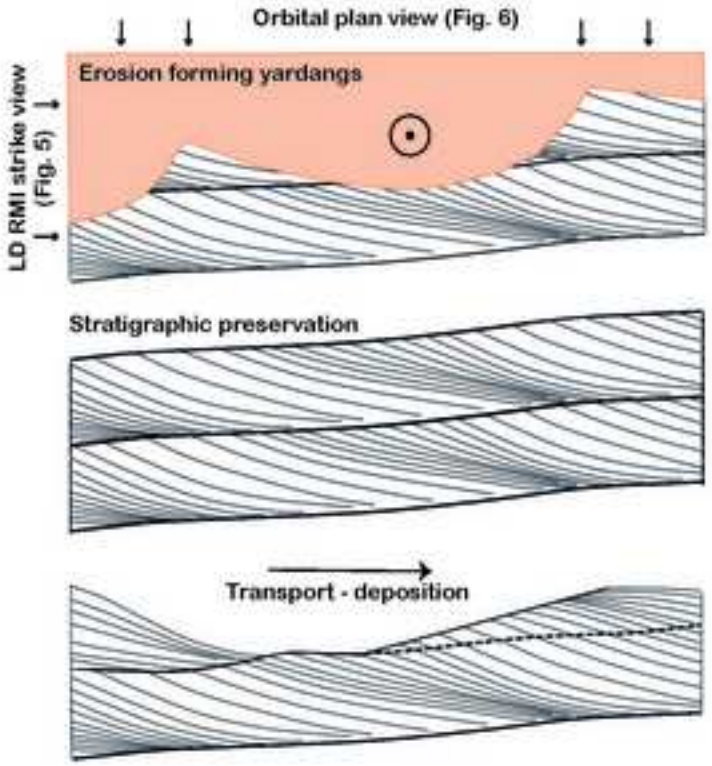

Dromart et al._Fig. 7

Figure

Click here to access/download;Figure;Fig_8_Resubmission.jpg

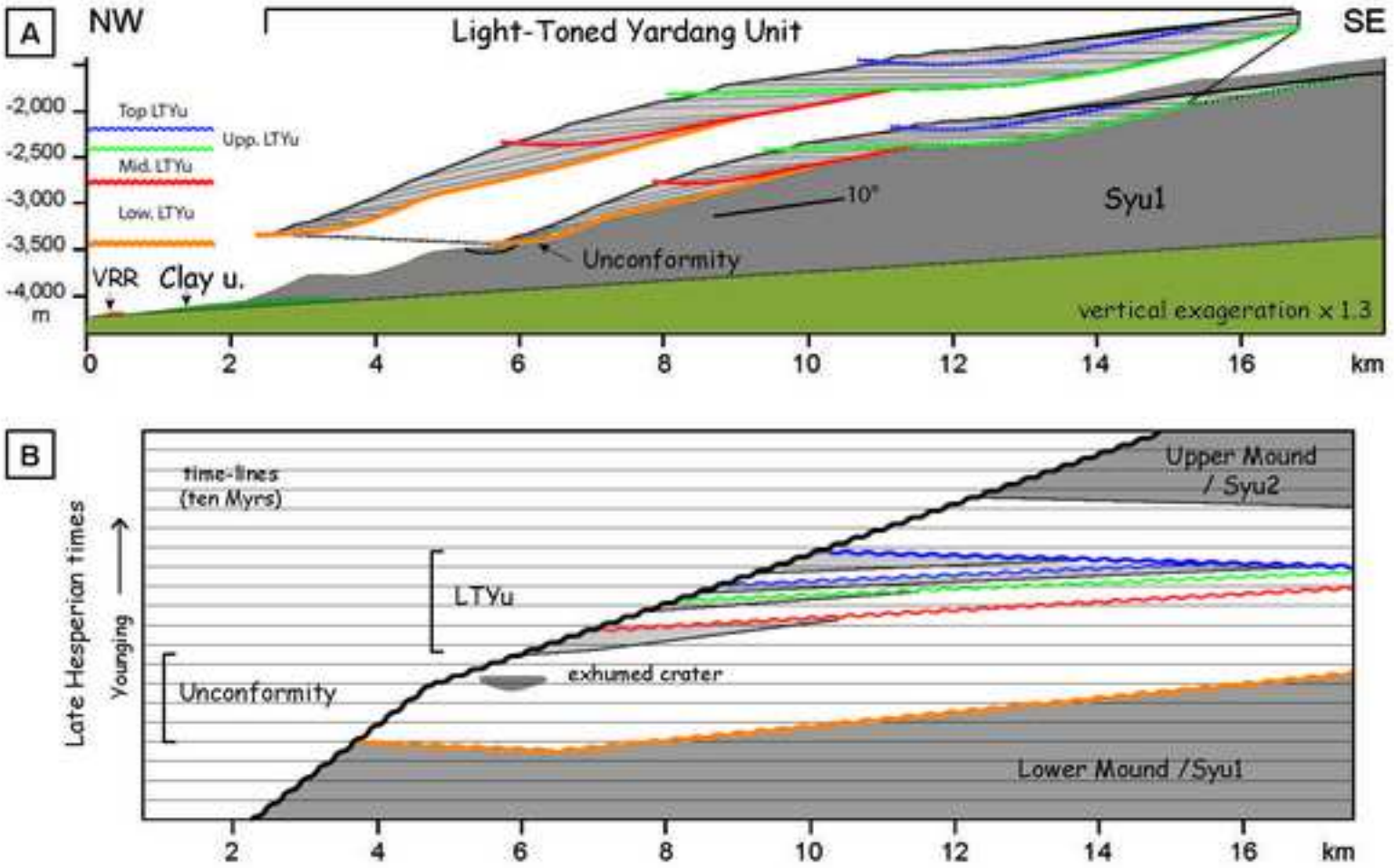

Dromart et al._Fig. 8

Figure

Click here to access/download;Figure;Fig_1N.jpg

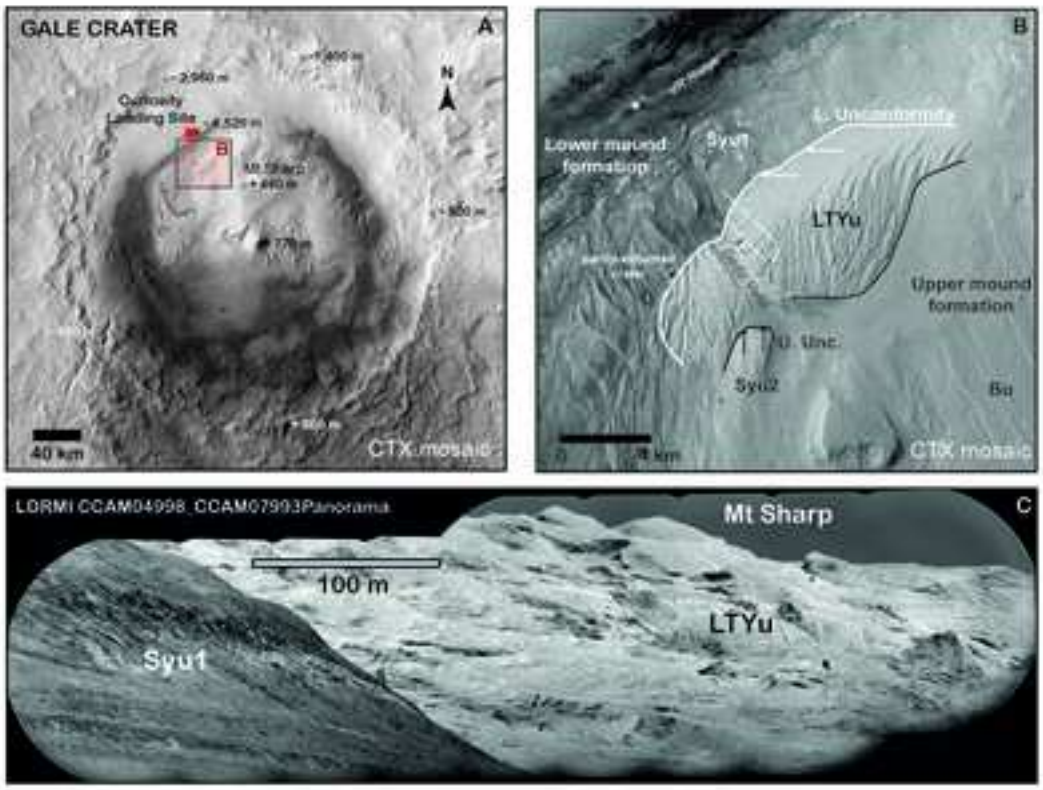

Dromart et al._Fig. 1

Figure

Click here to access/download;Figure;Fig_2N.jpg

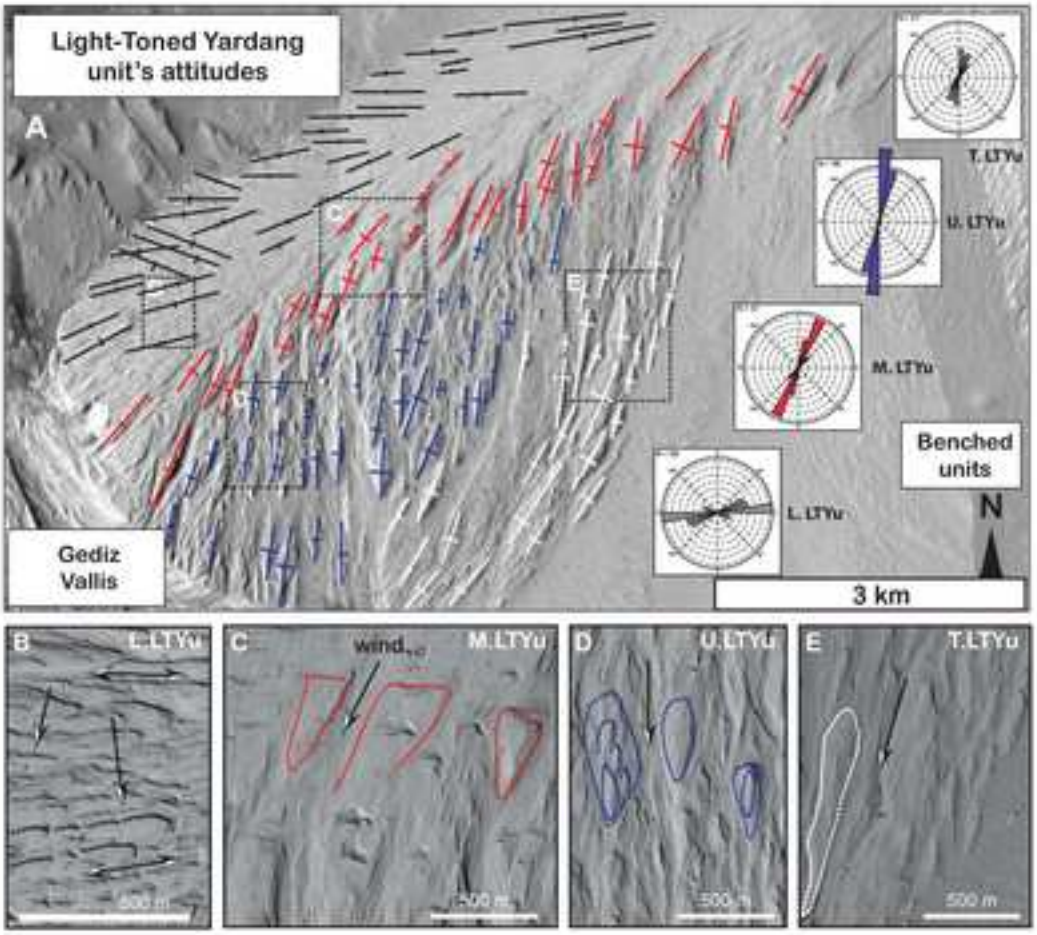

Dromart et al._ Fig. 2

Figure

Click here to access/download;Figure;Fig_3N.jpg

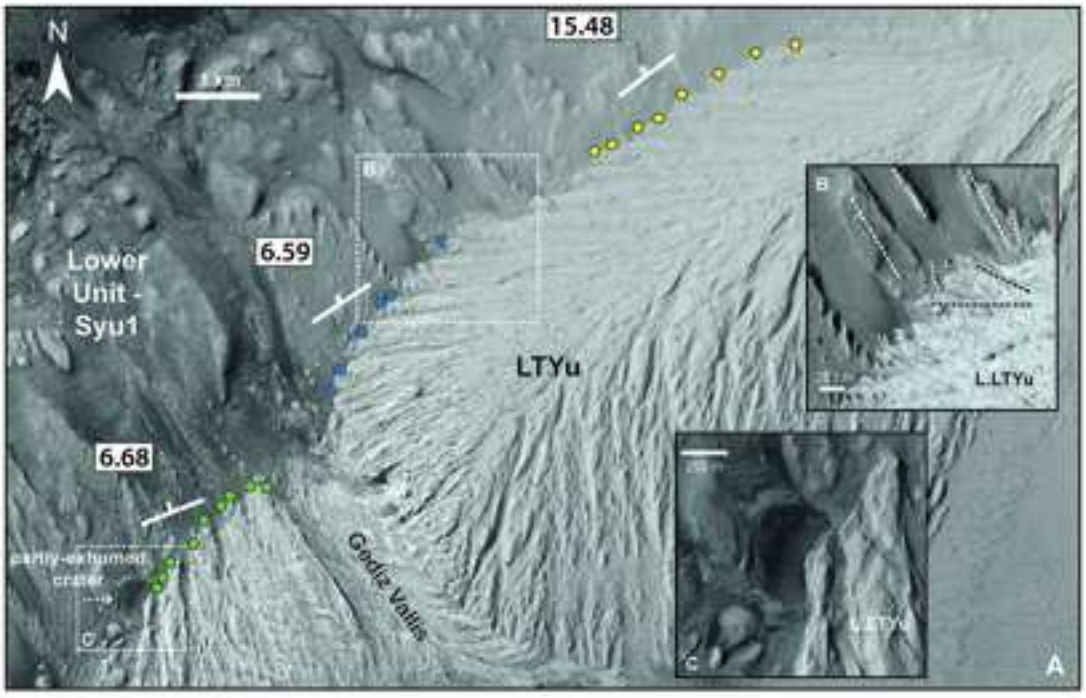

Dromart et al._Fig. 3

Figure

Click here to access/download;Figure;Fig_4N.jpg

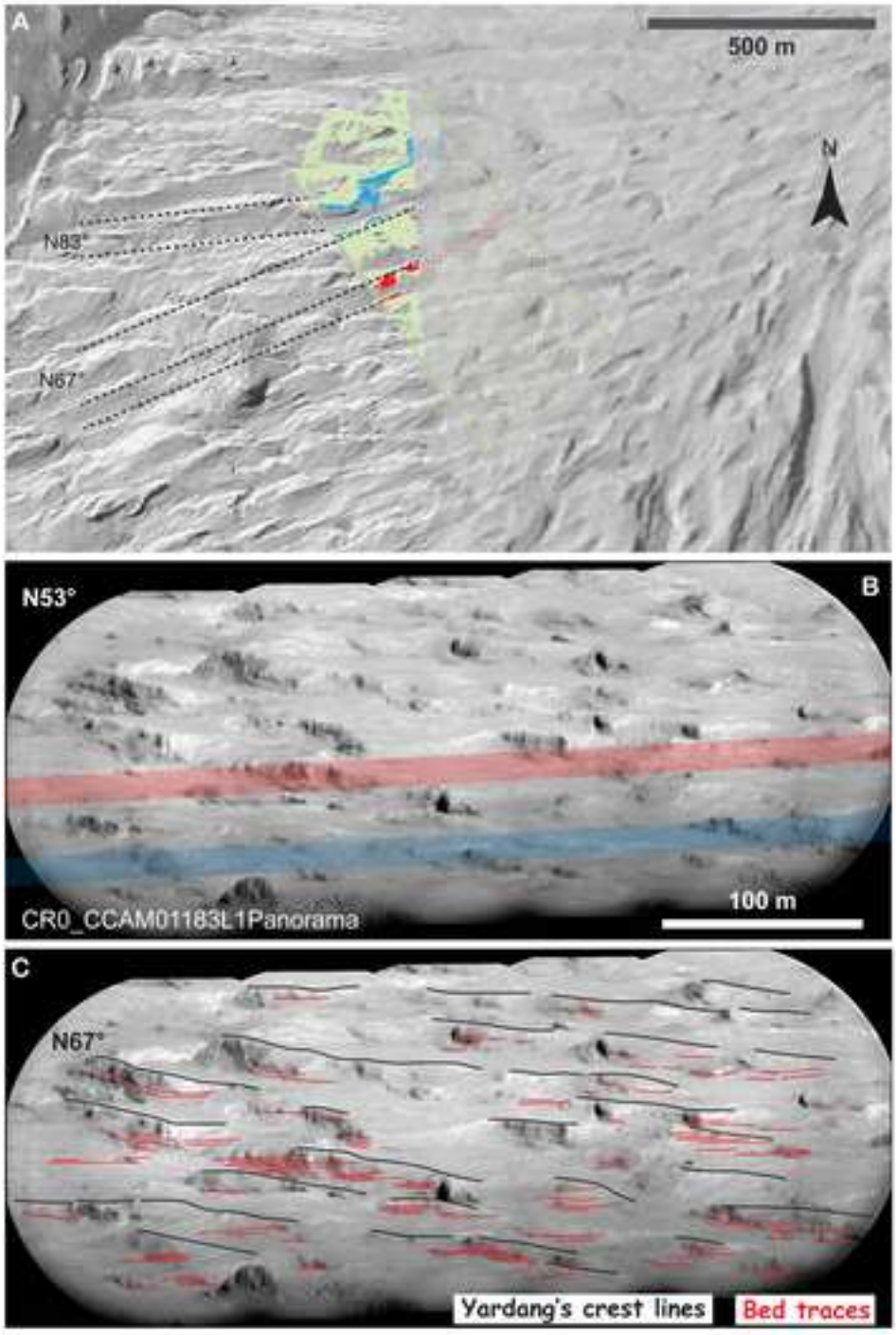

Dromart et al._Fig. 4

Figure

Click here to access/download;Figure;Fig_5N.jpg

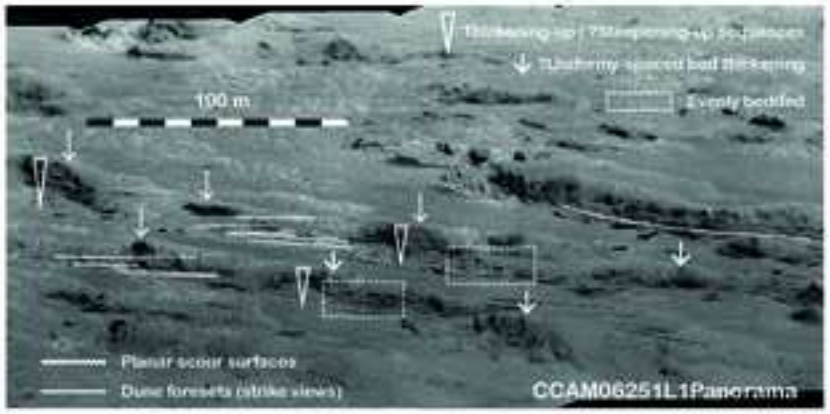

Dromart et al._Fig. 5

Figure

Click here to access/download;Figure;Fig_6N.jpg

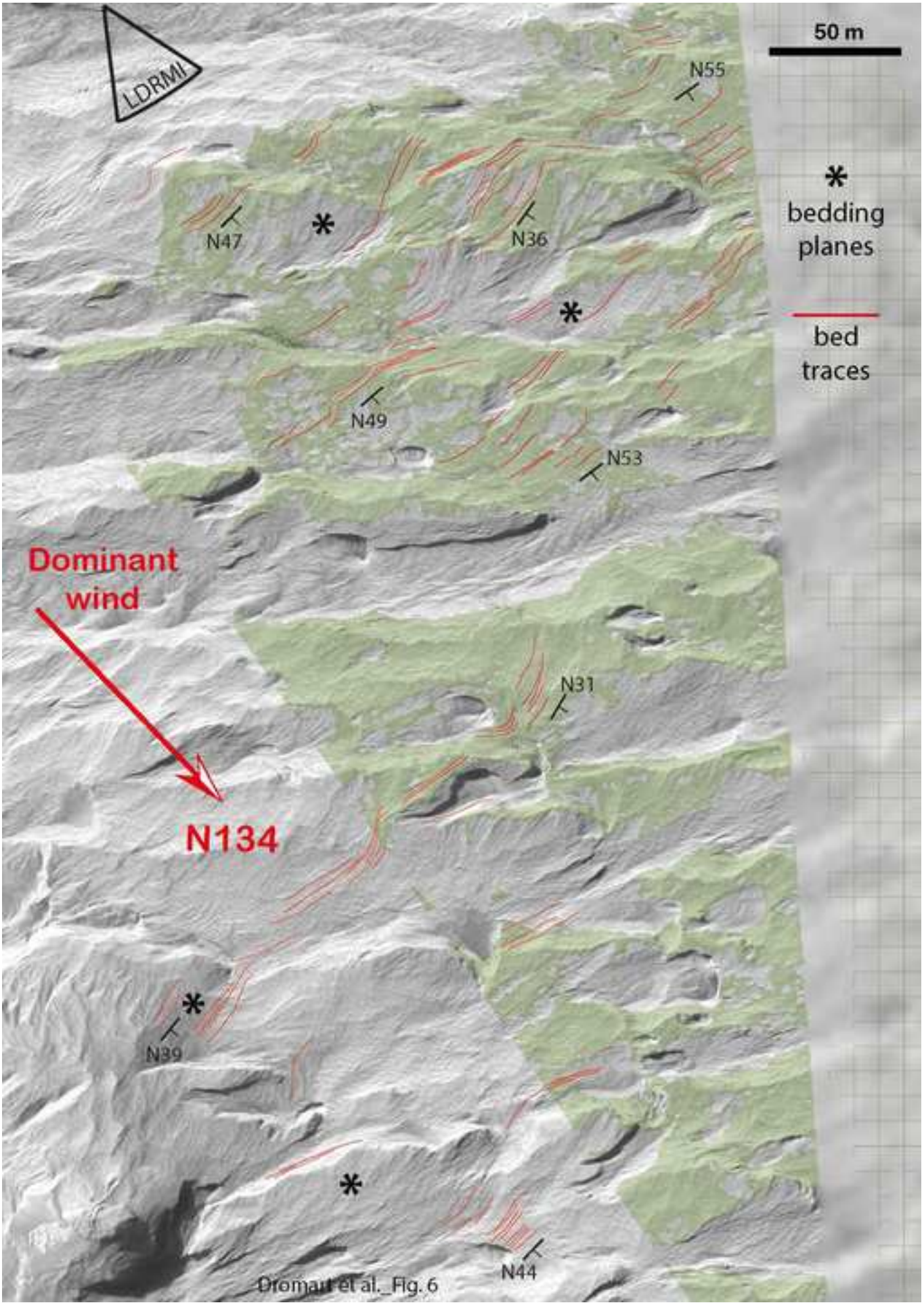

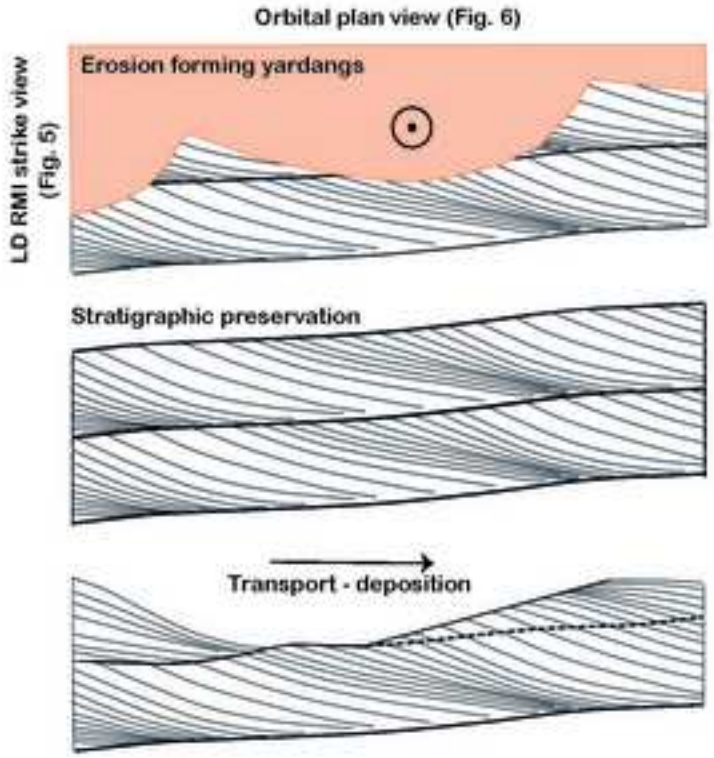

Dromart et al._Fig. 7

Figure

Click here to access/download;Figure;Fig_8N.jpg

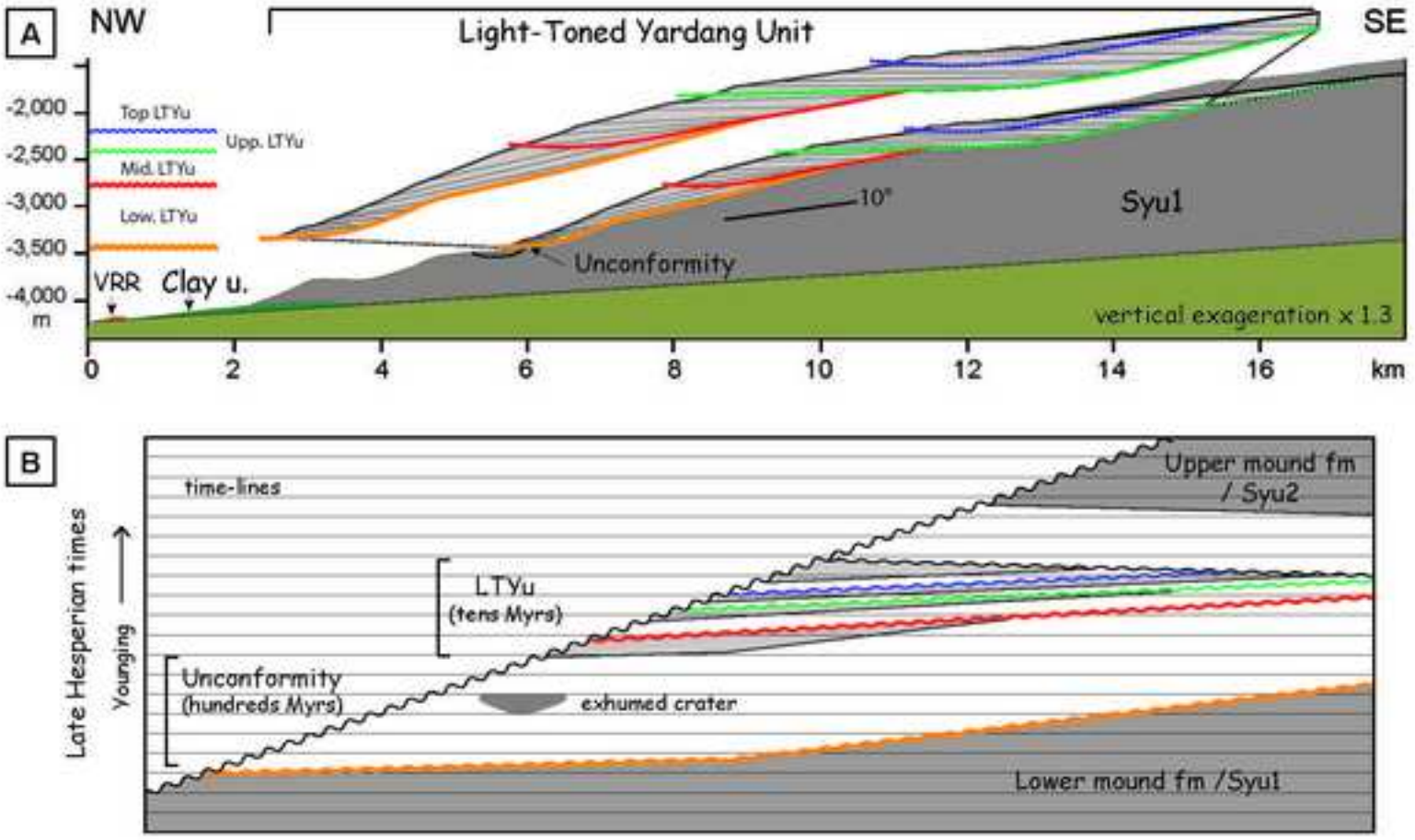

Dromart et al._Fig. 8

*Declaration of Interest Statement

Declaration of interests

☒ The authors declare that they have no known competing financial interests or personal relationships that could have appeared to influence the work reported in this paper.

☒The authors declare the following financial interests/personal relationships which may be considered as potential competing interests:

*Credit Author Statement

Author contributions

G.D. analyzed the image data, conceived and drafted the figures, conceived and wrote the manuscript. L.L. quantified the geometry of the LTYu basal bounding surface. W.R. projected the LD RMI mosaics as view sheds onto the DTMs. O.G. and SL carried out corrections of LD RMI mosaics. C. Q. calculated the lapse-time required for a surface to have a significant chance of having been impacted. N.M., D.R., J.L., S.M., H.N., P.P., L.S., R.W. contributed to the interpretation of the data and revisions of the manuscript.